Extreme Asteroids in the Pan-STARRS 1 Survey

McNeill, A., Fitzsimmons, A., Jedicke, R., Lacerda, P., Lilly, E., Thompson, A., Trilling, D. E., DeMooij, E., Hooton, M. J., & Watson, C. A. (2018). Extreme Asteroids in the Pan-STARRS 1 Survey. *Astronomical Journal*, *156*(6), Article 282. https://doi.org/10.3847/1538-3881/aaeb8c

Document Version:
Publisher's PDF, also known as Version of record

Queen's University Belfast - Research Portal:
[Link to publication record in Queen's University Belfast Research Portal](#)

Extreme Asteroids in the Pan-STARRS 1 Survey

Andrew McNeill[1,2], Alan Fitzsimmons[2] , Robert Jedicke[3] , Pedro Lacerda[2] , Eva Lilly[3], Andrew Thompson[2],
David E. Trilling[1] , Ernst DeMooij[4] , Matthew J. Hooton[2] , and Christopher A. Watson[2]
[1] Department of Physics and Astronomy, Northern Arizona University, Flagstaff, AZ 86011, USA; andrew.mcneill@nau.edu
[2] Astrophysics Research Centre, Queen's University Belfast, BT7 1NN, UK
[3] Institute for Astronomy, University of Hawaii at Manoa, Honolulu, HI 96822, USA
[4] School of Physical Sciences, Dublin City University, Glasnevin, Dublin 9, Ireland

Abstract

Using the first 18 months of the Pan-STARRS 1 survey, we have identified 33 candidate high-amplitude objects for follow-up observations and carried out observations of 22 asteroids. Four of the observed objects were found to have observed amplitude $A_{obs} \geqslant 1.0$ mag. We find that these high-amplitude objects are most simply explained by single rubble-pile objects with some density-dependent internal strength, allowing them to resist mass shedding even at their highly elongated shapes. Three further objects, although below the cutoff for "high amplitude," had a combination of elongation and rotation period which also may require internal cohesive strength, depending on the density of the body. We find that none of the "high-amplitude asteroids" identified here require any unusual cohesive strengths to resist rotational fission. Three asteroids were sufficiently observed to allow for shape and spin-pole models to be determined through light curve inversion. Asteroid 45864 was determined to have retrograde rotation with spin-pole axes $\lambda = 218° \pm 10°$, $\beta = -82° \pm 5°$ and asteroid 206167 was found to have best-fit spin-pole axes $\lambda = 57° \pm 5°$, $\beta = -67° \pm 5°$. An additional object not initially measured with $A_{obs} > 1.0$ mag, 49257, was determined to have a shape model that does suggest a high-amplitude object. Its spin-pole axes were best fit for values $\lambda = 112° \pm 6°$, $\beta = 6° \pm 5°$. In the course of this project, to date no large superfast rotators ($P_{rot} < 2.2$ hr) have been identified.

Key words: methods: observational – minor planets, asteroids: general – techniques: photometric

1. Introduction

We classify "extreme" asteroids based on their shape and spin state data. In this research, we define an "extreme asteroid" as an object rotating with a period shorter than the spin barrier ($P < 2.2$ hr), or an object with measured light curve amplitude $A \geqslant 1.0$ mag. This cutoff for "high amplitude" is largely arbitrary as to date there has been no work calculating a limit for rubble-pile asteroids accounting for angle of friction.

Figure 1 shows the rotation rate of all main belt asteroids plotted against diameter as recorded in the Light Curve Database (LCDB; Warner et al. 2009; last updated 2016 September 6). In this plot, we use only objects that have been assigned a quality code $U \geqslant 2-$. The quality code is assigned according to the reliability of the period result obtained. A value of $U = 1$ is assigned for a period determined from a light curve fragment that cannot be considered reliable. $U = 2$ corresponds to a result from partial light curves with a period value known within an uncertainty of 30%. $U = 3$ is assigned to accurate results from full light curve coverage (Warner et al. 2009).

In Figure 1, there is a clear cutoff in rotation rate at period $P \approx 2.2$ hr. This is approximately the critical spin rate for a strengthless body assuming a bulk density $\rho = 2500$ kg m^{-3}. The critical spin rate is defined as the speed of rotation required for the body to undergo rotational disruption. This suggests that most asteroids in the $0.2 < D < 10$ km size range are loosely bound, "rubble piles" of aggregate material with zero tensile strength.

1.1. Large Superfast Rotators

Large superfast rotators (SFRs) are defined as asteroids with diameter $D > 200$ m and with spin periods shorter than the spin barrier at $P = 2.2$ hr. This critical spin period is an estimate based on an average density value for asteroids and as such is not a hard cutoff; likewise, the diameter cutoff should be considered empirical. Literature values for the spin barrier range from $2 \leqslant P_{bar} < 2.2$ hr (Pravec et al. 2002), and at the time of writing, there were 20 objects in the LCDB not considered as SFRs but with rotation periods in this range. A higher than average density will allow for faster rotation without disruption and without requiring the object itself to be especially unusual. For this reason, we only consider objects with periods clearly shorter than $P = 2.2$ hr.

The first large SFR was discovered in 2001 by Pravec et al. (2002). Asteroid 2001OE84 was found to have a rotation period $P = 29.1909 \pm 0.0001$ minutes. The spectra obtained for this object suggested it to be a stony S-type object. Using the average albedo for this type of asteroid, its diameter is estimated at $D = 0.7$ km. Since the discovery of 2001OE84, there have been three further confirmed SFRs in the main asteroid belt along with a series of further candidates unconfirmed at the time this was written. Two of these have been identified by the Palomar Transient Factory (PTF; Chang et al. 2015, 2016). The confirmed SFRs are 2005UW163 and 1999RE88. 2005UW163 is an object in the inner main asteroid belt with an estimated mean diameter $D = 0.6 \pm 0.3$ km and a measured rotation period $P = 1.29 \pm 0.06$ hr. 1999RE88 is also found in the inner main belt with diameter $D = 1.9 \pm 0.3$ km and spin period $P = 1.96 \pm 0.01$ hr. Polishook et al. (2016) presented the final main belt SFR, 2000GD65 which is an S-type inner main belt object with $D = 2.3 \pm 0.6$km and $P = 1.9529 \pm 0.0002$ hr, making it the largest SFR known to date. A further Near Earth Asteroid (NEA) has also been found to have a superfast rotation period. Rozitis & Green (2014) show that 1950DA has diameter $D = 1.30 \pm 0.13$ km
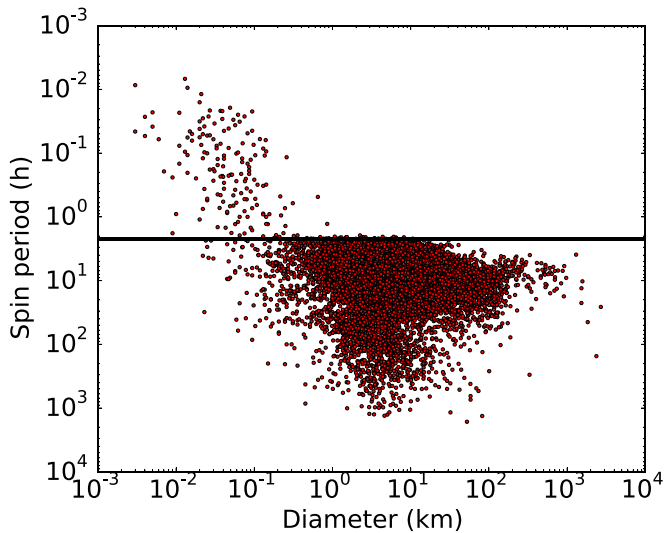
Figure 1. A plot of spin period against diameter for all objects in the Light Curve Database with quality code $\geqslant 2-$. The black line represents the "spin barrier" at $P = 2.2$ hr corresponding to the critical spin rate for an object with bulk density $\rho = 2500$ kg m^{-3}. Data from Warner et al. (2009; last updated 2016 September 6).

and rotation period $P = 2.12$ hr, only slightly below the critical spin rate stated here of $P = 2.2$ hr.

If an object were monolithic, then this would imply significant cohesive strength and would allow for faster rotation than the spin barrier. It is unlikely that any monoliths of this size remain intact in the asteroid belt without having undergone further collisional disruption; however, Polishook et al. (2017) have argued that a monolithic asteroid best explains the rotational behavior of 2001OE84, due to the high cohesive strengths that would be otherwise required to explain its short rotation period.

1.2. Highly Elongated Objects

Assuming the simplest case of a strengthless triaxial ellipsoid, there is a limit on the elongation the object can have before it becomes unstable and will undergo rotational fission (Jeans 1919). For a triaxial ellipsoid ($a \geqslant b \geqslant c$), this limit is at $b/a = 0.43$. Assuming a constant albedo for the asteroid and that all brightness variation is solely due to the projected shape of the body about its rotation axis, this corresponds to a light curve amplitude of $A \leqslant 0.9$ mag. However, there are several asteroids in the size range $0.2 < D < 10$ km, where objects are predominantly rubble piles, showing light curve amplitudes larger than this. Objects showing amplitudes significantly greater than this therefore cannot simply be assumed to be strengthless ellipsoids. As in the case of SFRs, a cohesive strength within the objects may have to be accounted for. Assuming rubble-pile objects to have some cohesive strength between their components may also allow for greater elongation.

It is not expected that asteroids in this size range can be approximated entirely as fluidic bodies. The use of hydrostatic equilibrium models in this case is not used to obtain accurate shape estimates for the objects; instead, this is a useful approximation that allows us then to account for the presence of cohesive strength in a body of this approximate shape and size.

A difference in the shape of the object may also account for this change. Although triaxial ellipsoids become unstable where $b/a < 0.43$, there is a sequence of equilibrium figures in the form of bilobed objects, which allow for a lower b/a while maintaining object stability (Chandrasekhar 1969; Descamps 2015). A bilobed object is described by the four axes $a \geqslant b \geqslant c \geqslant c'$, where c' is the minimum length of the c-axis at a "waist" between two larger lobes. The shape can best be described as like that of a dumb-bell or dog-bone.

We consider an object in the form of a Jacobi triaxial ellipsoid ($a > b \geqslant c$). As an object of this shape rotates around its axis, the projected area seen by an observer will change. This produces a double-peaked light curve when measured. The variation in the light curve can be used as a means of estimating the axis ratios of the asteroid, as shown in Equation (1), where A_{obs} represents the observed amplitude of the light curve, and θ is the latitude of the spin-pole axis. Assuming the spin axis of the object to be perpendicular to the orbital plane i.e., $\theta = 90°$, this reduces to Equation (2):

$$A_{\mathrm{obs}} = -2.5 \log \frac{b}{a} - 1.25 \log \frac{a^2 \cos^2 \theta + c^2 \sin^2 \theta}{b^2 \cos^2 \theta + c^2 \sin^2 \theta}, \quad (1)$$

$$A_{\mathrm{obs}} = -2.5 \log \frac{b}{a}. \quad (2)$$

The shapes of Jacobi ellipsoids can be determined by setting $a = 1$ and solving Equation (3) from Chandrasekhar (1969) for relative axis ratios b and c, where Δ is given in Equation (4):

$$a^2 b^2 \int_0^\infty \frac{du}{(a^2 + u)(b^2 + u)\Delta} = c^2 \int_0^\infty \frac{du}{(c^2 + u)\Delta}, \quad (3)$$

$$\Delta^2 = (a^2 + u)(b^2 + u)(c^2 + u). \quad (4)$$

If these a, b, and c values are known along with the angular rotation frequency of the object, ω, and assuming the object to have no internal strength, then the density of the asteroid may be estimated using Equation (5), where G is the gravitational constant and ρ is the density of the body in kg m^{-3}, assuming that the density of the object is constant throughout,

$$\frac{\omega^2}{\pi G \rho} = 2abc \int_0^\infty \frac{u du}{(a^2 + u)(b^2 + u)\Delta}. \quad (5)$$

Figures producing $A_{\mathrm{obs}} > 0.9$ mag would be unstable and will undergo mass loss during rotation unless some significant internal strength is assumed (Jeans 1919). Therefore, we assume that it is unlikely that our highest amplitude targets can be simply explained by an ellipsoid of this nature; however, some objects closer to the 1.0 mag selection criterion may be explained by Jacobi ellipsoids possessing cohesive strength, and thus we can consider this a valid shape for at least some of our targets.

However, to assume these rubble-pile objects to be simply fluid ellipsoids would be incorrect. Instead, we also account for the effect of the angle of sliding friction between the constituent parts of the rubble pile. To constrain the potential cohesive strengths of these rotating ellipsoids, we use a simplified form of the Drucker–Prager model, a stress–strain model commonly used in the study of geological materials (Alejano & Bobet 2012). The Drucker–Prager failure criterion is a three-dimensional model estimating the stresses within a geological material at its critical rotation state. The shear stresses on a body in three orthogonal xyz axes are dependent on the shape, density, and rotational properties of the body

(Holsapple [2007]):

$$\sigma_x = (\rho\omega^2 - 2\pi\rho^2 GA_x)\frac{a^2}{5}, \quad (6)$$

$$\sigma_y = (\rho\omega^2 - 2\pi\rho^2 GA_y)\frac{b^2}{5}, \quad (7)$$

$$\sigma_z = (-2\pi\rho^2 GA_z)\frac{c^2}{5}. \quad (8)$$

The three A_i functions are dimensionless parameters dependent on the axis ratios of the body:

$$A_x = \frac{c}{a}\frac{b}{a}\int_0^\infty \frac{1}{(u+1)^{3/2}\left(u+\frac{b^2}{a}\right)^{1/2}\left(u+\frac{c^2}{a}\right)^{1/2}}du, \quad (9)$$

$$A_y = \frac{c}{a}\frac{b}{a}\int_0^\infty \frac{1}{(u+1)^{1/2}\left(u+\frac{b^2}{a}\right)^{3/2}\left(u+\frac{c^2}{a}\right)^{1/2}}du, \quad (10)$$

$$A_z = \frac{c}{a}\frac{b}{a}\int_0^\infty \frac{1}{(u+1)^{1/2}\left(u+\frac{b^2}{a}\right)^{1/2}\left(u+\frac{c^2}{a}\right)^{3/2}}du. \quad (11)$$

The Drucker–Prager failure criterion defines the point at which the object will break up and is given in Equation ([12]), where k is the internal cohesive strength of the body, and s is a slope parameter dependent on the assumed angle of friction, ϕ. The expression for s is given in Equation ([13]),

$$\frac{1}{6}[(\sigma_x - \sigma_y)^2 + (\sigma_y - \sigma_z)^2 + (\sigma_z - \sigma_x)^2]$$
$$\leqslant [k - s(\sigma_x + \sigma_y + \sigma_z)]^2, \quad (12)$$

$$s = \frac{2\sin\phi}{\sqrt{3}(3 - \sin\phi)}. \quad (13)$$

Using a simple model based on this failure criterion, we determine the required cohesive strength as a function of density for each of the objects we have observed using input parameters determined from the observations. For the cases where high-density objects require cohesive strength, this is not necessarily to resist rotational fission, rather that some strength is required for the object to not undergo reshaping toward a more spherical shape. We use a Monte Carlo numerical simulation to determine solutions for a range of values using the uncertainties in each of the asteroid parameters to constrain the required cohesion of each object. Potential phase-angle opposition effects for different asteroid taxonomies are also accounted for in these uncertainties.

Holsapple ([2001]) showed that in their model most asteroids can be explained with an angle of friction of 15° or less. We assume this value in our calculations of density; it should be noted that these density values are simply estimates of the required density assuming this angle of sliding friction and should not be taken to be directly determined values.

1.3. Contact Binary or Bilobed Objects

Contact binary or bilobed objects have been discovered in almost every small-body population in the solar system. The abundance of binary systems can be relatively high with 10%–20% of Near Earth Object (NEO) and Kuiper Belt Object (KBO) populations showing evidence of binarity (Pravec et al. [2006]; Lacerda [2011]). A subset of the binary population exists as contact binary or bilobed systems. Three bilobed objects

have been identified in the Trojan family (Mann et al. [2007]) and two in the Kuiper Belt (Sheppard & Jewitt [2004]; Lacerda et al. [2014]). Contact binary or bilobed systems are important as by modeling their photometric light curves it is possible to obtain estimates of their bulk densities, assuming a rubble-pile structure. Spectroscopic, color, and albedo data allow the composition of an asteroid to be determined. With values of grain densities for different mineralogies known from meteorite studies, the bulk porosity of the object can be calculated. Also, non-contact binaries will be more readily collisionally disrupted than contact binaries. Hence, the ratio of bilobed bodies and non-contact binaries can be used to constrain the collisional statistics and history of asteroids in the main belt (Nesvorný et al. [2011]).

The formation mechanism of binary asteroids is dependent on the size of the system. Large binary objects ($D > 40$ km) are thought to be formed in collisional events while small binaries ($D < 20$ km) may also be explained by rotational fission due to the YORP effect (Bottke et al. [2002]; Pravec et al. [2010]). Benner et al. ([2006]) defined an asteroid contact binary as an asteroid consisting of two lobes in contact with a bimodal mass distribution that may once have been separate. Contact binary asteroids form whenever a separated binary spirals inward and the components collide "gently" due to either tidal interactions between the bodies or some angular momentum drain. This will occur when a separated binary has no possible stable synchronous orbit (Taylor & Margot [2011]).

Hektor is the most notable bilobed object in the solar system. It is a D-type Jupiter Trojan with $D = 233$ km (Cruikshank et al. [2001]; Usui et al. [2011]). Dunlap & Gehrels ([1969]) obtained light curve data for this object and found it to have amplitude $A_{obs} > 1.0$ mag. Cook et al. ([1971]) first proposed the idea that this object was best explained as a close or contact binary system rather than simply as an elongated object, a conclusion later backed up by Weidenschilling ([1980]). Recent studies have shown that >10% of Trojans may be contact binaries, a similar proportion to the KBO and NEO populations (Pravec et al. [2006]; Lacerda [2011]). However, no such abundance has been observed in the main asteroid belt. To date, six potential contact binary or bilobed objects have been found in the main belt (Ostro et al. [2000]; Marchis et al. [2005]; Descamps et al. [2007]; Shepard et al. [2015]). Only one of these objects falls in the size range primarily dealt with in this paper ($D < 10$ km). (3169) Ostro is a 5.15 ± 0.09 km object orbiting with a semimajor axis $a = 1.89$ au and with a rotation period $P = 6.509 \pm 0.001$ hr (Descamps et al. [2007]; Mainzer et al. [2011]). The light curve obtained for this object by Descamps et al. ([2007]) showed amplitude $A_{obs} = 1.20 \pm 0.05$ mag. Modeling the object as a Roche binary, they found a solution fitting both their own observations and previous apparitions for an object with a bulk density $\rho = 2600$ kg m^{-3}. At present, Ostro is the best candidate for a small main belt bilobed object.

Binary objects can produce much larger light curve variations than would be possible for a single object (Leone et al. [1984]). In this case, the light curve variation will be produced as the binary system orbits its barycenter, and the primary and secondary objects occult one another. As no eclipses are visible in the light curves of the high-amplitude asteroids observed, this suggests that if these objects are indeed binaries then they must be close binaries or potentially contact binaries. We first consider a simplified case of two spheres in contact.

The maximum light curve amplitude a bilobed object of this form can produce is $A = 0.75$ mag, well below the cutoff we set for "high-amplitude asteroids" ($A = 1.0$ mag). However, this is a highly simplified model as if we consider the components of the binary to be strengthless "rubble piles," then gravitational forces between the two will cause deformation of the bodies, allowing for even greater light curve amplitudes. To attempt to account for this deformation, we use the Roche binary approximation (Chandrasekhar 1963; Leone et al. 1984).

1.4. Roche Ellipsoid Constraints

Roche's problem deals with the effect of tidal forces acting between two bodies rotating around a common center of mass in a binary system. In this problem, the secondary component of the binary is treated as a rigid sphere and the primary's deformation to an equilibrium shape by gravitational forces determined, the resulting shape defined as a Roche ellipsoid, and then vice versa. Using the Roche binary approximation, we assume a binary system consisting of these two Roche ellipsoids. The resulting shape of each component can be calculated assuming two tidally locked components with the same rotation rate. In the case of close components with mass ratio $p \approx 1$, this approximation will introduce the greatest uncertainty into the result. In this case, the elongation of the primary and secondary will be underestimated, causing an underestimation of the light curve amplitude.

From Chandrasekhar (1963), the axis ratios of a Roche ellipsoid component with a given value of p can be determined from Equation (14), where a, b, and c are the lengths of the three axes of the ellipsoid, and p is the mass ratio. The parameters A_i are defined by Chandrasekhar & Lebovitz (1962) and are given in Equations (15)–(17),

$$\frac{(3 + p)a^2 + c^2}{pb^2 + c^2} = \frac{A_1 a^2 - A_3 c^2}{A_2 b^2 - A_3 c^2}, \tag{14}$$

$$A_1 = \frac{2}{a^3 \sin^3 \phi} \frac{1}{\sin^2 \theta} [F(\theta, \phi) - E(\theta, \phi)], \tag{15}$$

$$A_2 = \frac{2}{a^3 \sin^3 \phi} \frac{1}{\sin^2 \theta \cos^2 \theta} [E(\theta, \phi) - F(\theta, \phi)\cos^2 \theta$$
$$- \frac{c}{b} \sin^2 \theta \sin \phi], \tag{16}$$

$$A_3 = \frac{2}{a^3 \sin^3 \phi} \frac{1}{\cos^2 \theta} \left[\frac{b}{c} \sin \phi - E(\theta, \phi) \right]. \tag{17}$$

$E(\theta, \phi)$ and $F(\theta, \phi)$ are the standard incomplete elliptical integrals of the first and second kind given in Equations (18) and (19) with arguments θ and ϕ as defined in Equations (20) and (21),

$$E(\theta, \phi) = \int_0^\phi (1 - \sin^2 \theta \sin^2 \phi)^{\frac{1}{2}} d\phi, \tag{18}$$

$$F(\theta, \phi) = \int_0^\phi (1 - \sin^2 \theta \sin^2 \phi)^{-\frac{1}{2}} d\phi, \tag{19}$$

$$\theta = \sin^{-1} \left(\sqrt{\frac{a^2 - b^2}{a^2 - c^2}} \right), \tag{20}$$

$$\phi = \cos^{-1} \left(\frac{c}{a} \right). \tag{21}$$

The model of Lacerda & Jewitt (2007) sets three of the four parameters p, a, b, and c and interpolates to solve for the fourth. For the primary component, the major axis length is set to $a = 1$, and the axis length b is found for each combination of p and c between a minimum value and 1.00 in iterative steps of 0.01 (Lacerda & Jewitt 2007 use a mass ratio value q corresponding to $1/p$). This process is repeated using reciprocal values for the mass ratio to determine the shape of the secondary. For the axis ratios determined using this method, the square of the rotational frequency ω is given in units of $\pi G \rho$ by Equation (22), where ρ is the bulk density of the ellipsoid,

$$\frac{1}{1 + p} \frac{\omega^2}{\pi G \rho} = 2abc \frac{A_1 a^2 - A_3 c^2}{(3 + p)a^2 + c^2}. \tag{22}$$

Lacerda & Jewitt (2007) defined a valid Roche binary solution as when the (p, a, b, c) values for both the primary and secondary components give the same result when substituted into the right-hand side of Equation (22). A Roche binary system can produce a light curve amplitude of 1.5 mag, a factor of 2 larger than that for a binary composed of spherical bodies.

It is worth noting that to conclude any binarity or bilobed nature from a single set of light curve observations as described here is speculative. To determine the true shape of these objects, further observations would be required. Solutions calculated from Equation (22) should be considered viable but should not be mistaken for a definite statement on the binarity of these objects.

2. Pan-STARRS Data

The Pan-STARRS 1 1.8 m telescope on Haleakala contains a 1.4 gigapixel orthogonal transfer array CCD camera (GPC1) and covers a field of view of ~ 7 square degrees on the sky (Denneau et al. 2013; Chambers et al. 2016). GPC1 is made up of an 8×8 grid of OTA CCDs with each of these OTAs in turn comprising an 8×8 array of 590×598 10 μm CCDs (Tonry et al. 2012). The exposure time of observations is survey/filter dependent, and the CCD readout time is approximately 7 s (Magnier et al. 2013, 2016).

The $g_{P1} r_{P1} i_{P1} z_{P1} y_{P1} w_{P1}$ filter system used by the survey is similar to the Sloan–Gunn system; however, there are slight differences in wavelength range (Tonry et al. 2012). In this work we deal exclusively with data taken using the w_{P1}-band filter. The w_{P1} filter spans the combined range of the g_{P1}, r_{P1}, and i_{P1} filters, allowing detections down to 22nd magnitude.

The initial target list was constructed using the first 18 months of Pan-STARRS-1 survey data. We consider objects in the range $2 < a < 4$ au with an upper limit of $e < 0.35$ to prevent any contamination of the sample by NEOs. We consider detections with a photometric uncertainty $\sigma < 0.05$ mag. A maximum change of $\Delta m < 1.2$ mag was allowed between detections as it would be unphysical for an asteroid to show variations greater than this due to rotation on a 15 minute timescale. Using both the time between detections and the difference in brightness, the absolute rate of change in magnitude was calculated for each detection pair within a tracklet.

The data set was filtered down to only include objects that showed three or more values of rate of change in magnitude

$|\dot{m}| > 0.3$ mag per 15 minute spread across two or more tracklets. We also favored objects which showed similar variations in the later data (2012 May onwards). This gave a list of 38 potentially interesting targets for follow-up. In order to further reduce the likelihood that the large variations for these objects were caused by bad pixels or background contamination, each image for the 38 targets was manually inspected. Using this method, it was found that five of the objects had changes in brightness that were caused by mechanisms other than rotation, and hence these were removed from the target list.

The target list was divided into primary and secondary targets according to the largest observed change in brightness. Primary targets were defined as those showing absolute rates of change in magnitude $|\dot{m}| > 0.6$ mag per 15 minutes. There were 10 primary targets defined this way. All remaining objects were named secondary targets.

3. Observations

In the course of this project, 22 nights were spent observing on the Isaac Newton Telescope (INT) and the New Technology Telescope (NTT). We were supported by follow-up observations throughout the duration of the project using the University of Hawaii 2.2 m telescope.

3.1. Isaac Newton Telescope

The 2.5 m INT is located at the Roque de los Muchachos Observatory on La Palma in the Canary Islands where it is a part of the Isaac Newton Group. The instrument used for the observations within this project was the Wide Field Camera (WFC). The WFC is a four-chip mosaic comprising EEV 2048×4100 pixel CCDs. The CCDs have a pixel size of 13.5 μm giving a pixel scale of $0\rlap{.}''33$ per pixel. Images taken using the INT are recorded as multi-extension fits files with an extension for each of the four CCDs. For the purposes of this investigation, we were only concerned with the data on the central CCD, CCD4.

Our initial observing strategy was to obtain at least 3.3 hr of coverage on a single object, allowing for at least 1.5 rotations of a superfast rotator. These observations were carried out using the Sloan r filter with fast readout (a readout time of 29 s) and over an exposure time selected to ensure the object's motion did not exceed $0\rlap{.}''5$. In poor seeing, we increased this exposure time to ensure we obtained the required signal-to-noise ratio. We later adjusted this observing strategy to observe multiple targets in order to obtain maximum coverage of our target list. For this method, we selected two or three visible targets and cycled between them in intervals of 10–20 minutes.

3.2. New Technology Telescope

The 3.58 m ESO NTT is located at La Silla in the Atacama Desert, Chile. The NTT is a Ritchey–Chrétien telescope on an altazimuthal mount. The instruments on the NTT are mounted on its two Nasmyth foci. The instrument used in this investigation was the ESO Faint Object Spectrograph and Camera (EFOSC2). The EFOSC2 CCD is 2048×2048, and the field of view is $4\rlap{.}'1 \times 4\rlap{.}'1$ with a pixel scale of $0\rlap{.}''12$ per pixel. The observations presented here were taken using the Sloan r filter and with "normal" readout speed (40 s). For this we used 2×2 binning.

As with the INT observations, exposure times were calculated for each object to obtain maximum signal-to-noise ratios while keeping the asteroid's motion in that interval to $<0\rlap{.}''5$. The same observing strategies were used for the NTT observations as for the INT.

4. Analysis

To search for periodicities in the brightness variations of the observed asteroids, we use the Lomb–Scargle method to generate periodograms. We favor the Lomb–Scargle method in this case as we have irregularly spaced data, which this method can easily handle unlike, e.g., fitting a Fourier model, which would require regularly spaced data.

The main drawback of the original Lomb–Scargle periodogram is that it does not account for uncertainties in the input data. As we are dealing primarily with high-quality photometric data measured from high-amplitude objects, this is unlikely to affect our result too much. However, we still elected to use the "Generalized Lomb–Scargle Periodogram" (Zechmeister & Kürster 2009), which takes these uncertainties into account. This method also fits for the mean of the observed data rather than simply assuming that it is identical to that of the fitted sine curve, an assumption made by the initial form of the Lomb–Scargle periodogram.

To estimate the uncertainty in the period obtained, we use Equation (23) (Horne & Baliunas 1986). In this equation, A is the light curve amplitude, T is the total time spread of the data set, and σ_N is the variation of the noise in the data. Assuming that the variation in the asteroid light curves is due to the rotation of the object, we assume the most likely period to be twice the best-fit period from our Lomb–Scargle periodogram. This will produce the expected double-peaked light curve from rotation:

$$\delta\omega = \frac{3\pi\sigma}{2\sqrt{N}\,TA}. \tag{23}$$

For each object, we consider the following cases as potential shape solutions: a single ellipsoidal rubble-pile object and a binary or bilobed approximation. For the case of a single elongated object, we use Equations (3) and (4) to obtain a Jacobi ellipsoid shape solution for the axis ratios of the body. A density for this strengthless solution can then be obtained using Equation (5). In addition to the uncertainty in this value due to the uncertainties in the shape and spin properties of the object, we also apply an uncertainty due to internal friction. Following the method of Holsapple (2001), we obtain a range of densities for which the Jacobi shape solution applies assuming an angle of friction $\phi_F \leqslant 15°$. The required strength of an object in these uncertainty ranges can then be determined using Equations (6)–(13). This strength value provides a sensible upper limit on the internal strength of these objects as a lower angle of friction than this in an asteroid is unlikely.

For the case of a bilobed or contact binary as detailed in Sections 1.3 and 1.4, we use the model of Lacerda & Jewitt (2007) to obtain the shape and density for this configuration. We also obtain solutions where possible for bilobed objects along the bilobed equilibrium sequence as defined by Descamps (2015).

In cases where there is a clear unambiguous solution for a single elongated object, we favor this shape configuration. For those objects where the solution for a single elongated object requires unusual density or strength, we also consider binary or

bilobed solutions to be valid. It should be emphasised, however, that from light curve data alone, any binary or bilobed solutions should be considered speculative.

5. Photometry

Data reduction and photometry were performed using the IRAF software package *apphot* (Davis 1999). For each night of observation, at least 30 bias frames were taken and combined into a single average frame for bias subtraction. Each night at twilight, sky exposures were taken and combined and normalized to generate a flat field image.

In this work, we use differential photometry rather than absolute photometry. For these observations, however, we had access to the stellar magnitudes cataloged by the PS1 3π survey, which measured the magnitudes of all stars in its sensitivity range above decl. $-30°$. This survey data was part of the first public data release in late 2016 (Flewelling et al. 2016; Magnier et al. 2016). With this data, differential photometry becomes straightforward and allows us to obtain accurate measurements even in non-photometric conditions.

Due to the relatively fast motion of the asteroids observed, it was impossible to use the same stars on multiple nights so instead it was necessary to select suitable different stars for each night. At least five stars were used in each set of observations to minimize the risk of contamination by stellar phenomena, e.g., variability. To ensure none of our background stars will affect our data adversely, we plot the difference in brightness between each combination of two background stars and remove any stars showing significant variation with time. Any other factors acting on the brightness of both the asteroid and background stars, e.g., cloud cover or atmospheric effects, can be assumed to affect all bodies equally.

Measurements were taken with circular apertures centered around both the target asteroid and the background stars. The radius of this aperture was chosen based on the FWHM of the background stars in pixels to maximize the obtained signal-to-noise ratio (Howell 1989). For all targets observed at decl. $>$ $-30°$, we are able to make use of Pan-STARRS 3π survey data to obtain accurate magnitudes for these background stars, for those targets observed with the NTT at decl. $<-30°$, we made use of the Gemini South GMOS-S Photometric Standard Star Fields.

Light curve amplitude is dependent on the phase angle of the observations. Scattering effects and increased shadowing at high phase angles will cause light curve minima to appear fainter and hence causes the light curve amplitude to be increased. This can lead to an overestimation of the elongation of an object. Zappala et al. (1990) demonstrated a linear relationship between the apparent amplitude of a light curve A_{obs} and its actual amplitude $A(\alpha = 0°)$ for phase angles $\alpha \leqslant 40°$. This is given in Equation (24), where s is a taxonomy-dependent slope parameter,

$$A(\alpha = 0°) = \frac{A_{\mathrm{obs}}}{1 + s\alpha}. \quad (24)$$

All reported light curve observations in this project were made in the main asteroid belt and hence fall within this α domain, allowing Equation (24) to be used. As the photometric data obtained as part of this project alone is not enough to determine the taxonomy of any of our target objects, we use a conservative value of $s = 0.015$ mag deg^{-1} in each case.

6. Observational Results

A summary of the orbital and observational properties of each asteroid discussed in this section is presented in Tables 1–3.

6.1. 39684 (1996 PD8)

The Lomb–Scargle periodogram calculated from these observations is given as Figure 2.

The periodogram finds a best-fit rotation period of $P_r = 4.836 \pm 0.016$ hr. The measured light curve folded to this rotation period showed an amplitude of 1.29 ± 0.02 mag and is given in Figure 3. Accounting for phase angle, this amplitude scales to 1.17 ± 0.02 mag.

For these values, we find a best result for a Jacobi ellipsoid with axis ratios $1:0.34 \pm 0.01:0.29 \pm 0.01$ and density $\rho = 2600 \pm 50$ kg m^{-3}. The elongation of this object would imply that if it were a rubble pile, it would be unstable and mass loss would occur. For this object to be stable, significant cohesive strength would be required. From the work of Holsapple (2001), we find a range of densities allowed for an ellipsoid of this shape assuming $\phi = 15°$ of $1900 < \rho < 5900$ kg m^{-3}.

The Roche model produced a lower limit fit for this object of density $\rho = 4400 \pm 200$ kg m^{-3}. Considering the porosity required for Roche deformation, this is an extremely high density value approaching the maximum we defined for asteroids for porosity $\sim 55\%$. This density seems implausible for the case of a Roche tidally distorted bilobed object, although we cannot entirely rule it out.

For objects along the bilobed equilibrium sequence rotating with $P_r = 4.840 \pm 0.006$ hr, we obtain density values $2900 < \rho < 5900$ kg m^{-3} across the range of Ω values. Here, the only solutions that give densities that could be plausible are those close to the Jacobi bifurcation ellipsoid, i.e., $c' \approx c$. These solutions may produce the observed light curve, and we must consider them a possible solution.

In summary, we find the most viable solution is obtained for a triaxial ellipsoid potentially with some degree of cohesive strength. We find potential solutions for objects with density $1900 < \rho < 5900$ kg m^{-3}, axis ratio $1:0.34 \pm 0.01:0.29 \pm 0.01$, and internal cohesive strength 50–530 Pa. There are some solutions on the bilobed equilibrium sequence that also may explain this asteroid's light curve; however, there is no evidence at this time to suggest that this is a more likely solution than a simple ellipsoid.

6.2. 45864 (2000 UO97)

This object represents the most well-observed target from our initial list. The generalized Lomb–Scargle periodogram for this is given in Figure 4.

Figure 4 shows a best-fit rotation period of $P_r = 5.135 \pm 0.001$ hr. Light curves folded to this period from the data are given in Figures 5–8.

Since these observations were carried out, Ďurech et al. (2016) have calculated a period for this object from sparse archival data and obtained a value of 5.13544 ± 0.00001 hr, in agreement to within uncertainties of our observed value.

The maximum amplitude observed for this object was found to be 1.61 ± 0.01 mag, an extremely large variation for a main belt asteroid of this size (~ 4.3 km). Adjusting for the relatively high phase angle of these observations, the real amplitude is closer to 1.15 ± 0.01 mag. In Figures 7 and 8, the corrected

Table 1
Table of Observations

Object	Date (UT)	Obs. Hours	Images	Filter	Telescope	r (au)	Δ (au)	m_V	α (deg)
39684	2015 Apr 29th	2.7	85	r	INT	3.08	2.13	18.83	8
39684	2015 Apr 30th	3.8	138	r	INT	3.08	2.13	18.81	7
39684	2015 May 1st	4.6	60	r	INT	3.08	2.12	18.79	7
39684	2015 May 2nd	4.7	142	R	UH2.2 m	3.08	2.11	18.77	7
45864	2015 Jan 22nd	2.0	107	R	UH2.2 m	2.16	1.83	18.30	27
45864	2015 Jan 27th	2.6	127	R	UH2.2 m	2.15	1.90	18.38	27
45864	2015 Jan 28th	2.9	144	R	UH2.2 m	2.15	1.91	18.39	27
45864	2016 Jan 15th	1.9	104	R	UH2.2 m	2.20	2.06	18.57	26
45864	2016 Jan 18th	1.7	120	R	UH2.2 m	2.20	2.03	18.54	27
45864	2016 Apr 15th	1.4	41	r	INT	2.30	1.31	16.94	5
45864	2016 Apr 16th	1.5	20	r	INT	2.30	1.31	16.92	5
45864	2016 May 6th	4.2	23	r	UH2.2 m	2.33	1.35	17.16	8
45864	2016 May 27th	2.7	35	r	INT	2.35	1.49	17.71	17
45721	2015 Apr 29th	3.4	96	r	INT	4.04	3.07	19.03	4
45721	2015 Apr 30th	5.5	81	r	INT	4.04	3.07	19.04	4
18018	2015 May 1st	4.3	79	r	INT	2.19	1.45	18.08	22
18018	2015 May 6th	3.0	106	r	WHT	2.19	1.50	18.19	23
18018	2015 Jun 9th	1.4	55	R	UH2.2 m	2.21	1.90	18.83	27
18018	2015 Jun 10th	1.3	52	R	UH2.2 m	2.21	1.91	18.85	27
18280	2016 Jan 16th	1.1	19	r	INT	2.12	1.35	17.50	21
18280	2016 Jan 16th	1.8	63	R	UH2.2 m	2.12	1.35	17.50	21
18280	2016 Jan 18th	0.5	15	r	INT	2.12	1.36	17.55	21
18280	2016 Jan 19th	2.9	191	R	UH2.2 m	2.12	1.37	17.57	22
206167	2015 Jul 18th	4.5	57	r	NTT	2.70	1.83	20.26	14
206167	2015 Jul 23rd	2.1	54	R	UH2.2 m	2.69	1.87	20.35	15
206167	2015 Jul 24th	2.3	77	R	UH2.2 m	2.69	1.88	20.37	16
49257	2015 Jul 17th	2.6	108	r	NTT	2.36	2.17	19.62	26
49257	2015 Jul 18th	2.7	120	r	NTT	2.36	2.16	19.61	26
49257	2015 Jul 23rd	1.7	58	R	UH2.2 m	2.36	2.10	19.54	26
49257	2015 Sep 18th	4.3	172	R	UH2.2 m	2.35	1.50	18.50	16

Table 2
Table of Orbital and Physical Properties of High-amplitude Asteroids

Object	a (au)	e	i (°)	H	Albedo	D (km)
39684	2.92	0.07	2.89	14.2	0.12 ± 0.04[a]	4.5 ± 1.0
45864	2.31	0.10	5.89	14.1	0.35 ± 0.05[a]	4.3 ± 0.2
45721	3.80	0.07	1.02	13.2	0.10 ± 0.01[a]	8.5 ± 0.2
18018	2.20	0.05	6.19	14.5	0.30 ± 0.08[a]	3.3 ± 0.4
18280	2.42	0.13	7.54	14.3	0.21 ± 0.10[b]	4.5 ± 1.2
206167	2.78	0.17	2.72	16.0	0.17 ± 0.08[b]	2.3 ± 0.6
15613	2.57	0.11	12.8	13.9	0.23 ± 0.03[a]	6.0 ± 0.1
49257	2.62	0.10	5.66	14.9	0.27 ± 0.08[a]	3.1 ± 0.3

Notes.
[a] *WISE*/NEOWISE albedos (Masiero et al. 2011).
[b] Average albedo for 0.5 au annuli of main asteroid belt (McNeill et al. 2016).

Table 3
Summary Table of Rotational Properties of High-amplitude Asteroids

Object	P (hr)	A (mag)	$A_{0°}$ (mag)
39684	4.836 ± 0.016	1.29 ± 0.02	1.17 ± 0.02
45864	5.135 ± 0.001	1.61 ± 0.01	1.15 ± 0.01
45721	6.00 ± 0.06	1.11 ± 0.07	1.05 ± 0.07
18018	5.608 ± 0.002	1.33 ± 0.03	1.00 ± 0.03
18280	3.808 ± 0.008	1.15 ± 0.05	0.87 ± 0.05
206167	3.944 ± 0.002	1.05 ± 0.15	0.86 ± 0.12
15613	3.3 ± 0.4	1.02 ± 0.02	0.78 ± 0.02
49257	3.3896 ± 0.0002	0.80 ± 0.05	0.58 ± 0.05

amplitudes of the light curve were found to be 0.93 and 0.97 mag, respectively. This change is potentially due to the change in orbital geometry between the sets of observations.

For an object with this rotation rate and showing this magnitude variation, we find that for this to be explained by a Jacobi ellipsoid would require an object with axis ratios 1:0.35 ± 0.01:0.29 ± 0.01 and a bulk density $\rho = 2300 \pm 50$ kg m^{-3}. The albedo of this object is too high (~0.35) a value for the most abundant S and C classes of asteroids (Mainzer et al. 2011). We consider the possibility that this

object is instead an E-type enstatite chondritic asteroid. If this object were a rubble-pile Jacobi ellipsoid, the axis ratios required for this object mean that the object is much too elongated to exist as a single object without undergoing mass loss, suggesting that the object would have to be monolithic. The internal friction acting between the solid aggregate of a rubble pile allows it to withstand breakup to a greater extent than a fluid body, although its strength will still be considerably less than that of a coherent body.

Holsapple (2001, 2004) derived limits on the equilibrium configurations for an ellipsoid with no tensile strength, modeling them as elastic-plastic materials using a Mohr–Coulomb yield
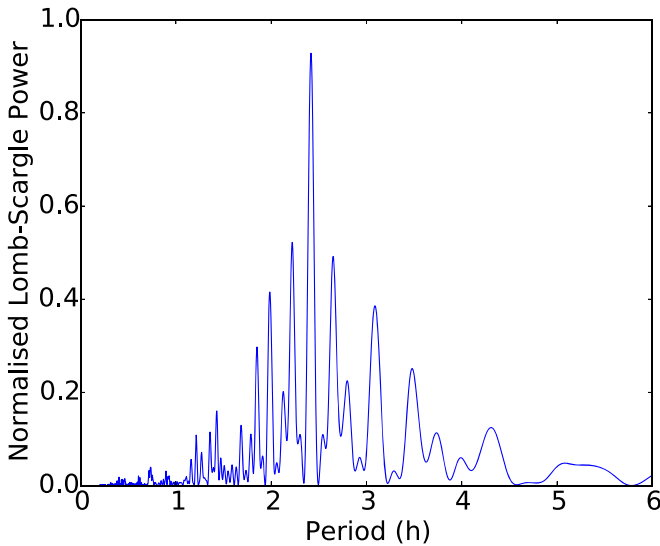
Figure 2. The Lomb–Scargle periodogram generated from the light curve data of 39684.
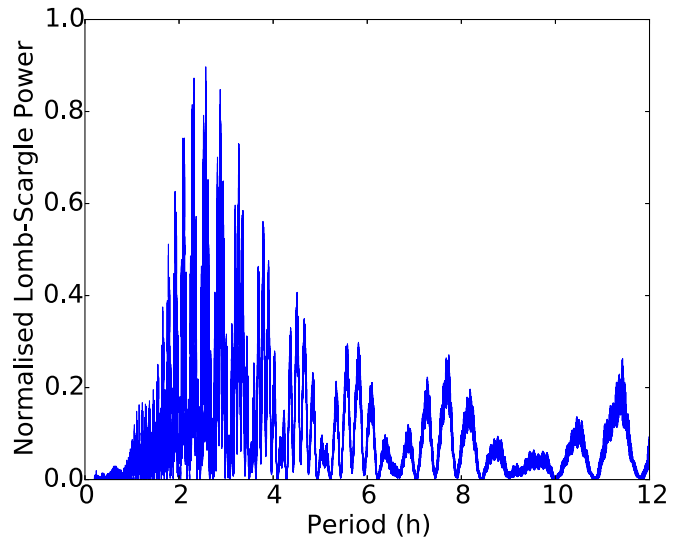

Figure 4. The Lomb–Scargle periodogram generated from the light curve data of 45864 from 2015 January.
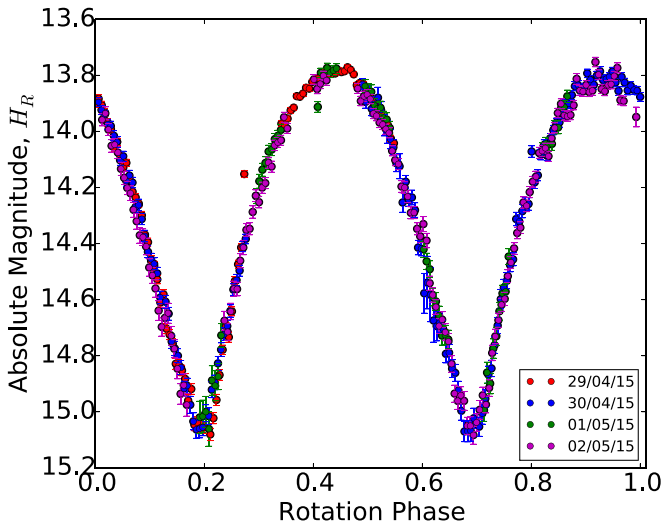

Figure 3. A light curve constructed from photometric data from observations of asteroid 39684 using the Isaac Newton Telescope in 2015 April and May and phased to the determined rotation period $P_r = 4.836 \pm 0.016$ hr.
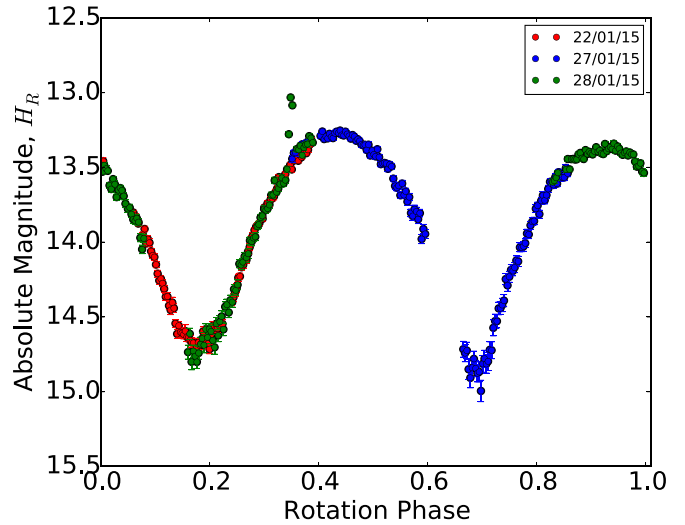

Figure 5. A light curve constructed from photometric data from observations of asteroid 45864 using the University of Hawaii 2.2 m Telescope in 2015 January and phased to the determined rotation period $P_r = 5.135$ hr.

model dependent on the angle of friction, ϕ_F. Sharma et al. (2009) showed that for most large asteroids, the angle of friction $\phi_F < 5°$. Taking the Jacobi ellipsoid shape of 1:0.35:0.29 and using the scaled spin rate $\left(\Omega = \frac{\omega}{\sqrt{G\rho}}\right)$ versus axis ratio (b/a) plots of Holsapple (2001), there is no equilibrium figure for an object of this shape rotating with this rotation period where $\phi_F < 5°$. Holsapple (2001) shows that all asteroids put into their model have $\phi_F < 40°$ with most having $\phi_F < 15°$. Taking this boundary of $\phi_F < 15°$, we find a range of densities that an ellipsoid figure of equilibrium can take for an object with 45864's rotation period and obtained axis ratios. The range obtained was $1600 < \rho < 5200 \text{ kg m}^{-3}$.

Using the Drucker–Prager yield model (Equation (12)) and the calculated densities, we constrained a cohesive strength in the range 0–130 Pa (assuming an angle of friction $\phi_F = 15°$). A strengthless solution of a Jacobi ellipsoid is present at around 2300 kg m^{-3} as predicted earlier in this section. The lower end

of this density range represents the most plausible values of bulk density for a rubble pile.

The result obtained from the method described by Lacerda & Jewitt (2007) gave a lower limit density of $3900 \pm 200 \text{ kg m}^{-3}$. This is an extremely high density and is again difficult to reconcile with the theory of asteroids being rubble piles. At a porosity of 50%, this bulk density would require a grain density approximately that of iron. As the assumption that the object is a binary consisting of two Roche ellipsoids does not provide a believable solution, we must consider alternative explanations. For this obtained density to be correct, the object would have to be a bilobed object consisting of two solid components. As these bodies would not be deformed by tidal forces, they would be closer to spherical components than Roche ellipsoids. Objects of this nature could not produce a light curve amplitude as great as the one observed due to shape alone, and it would be unlikely that albedo variegation could make up this large difference.
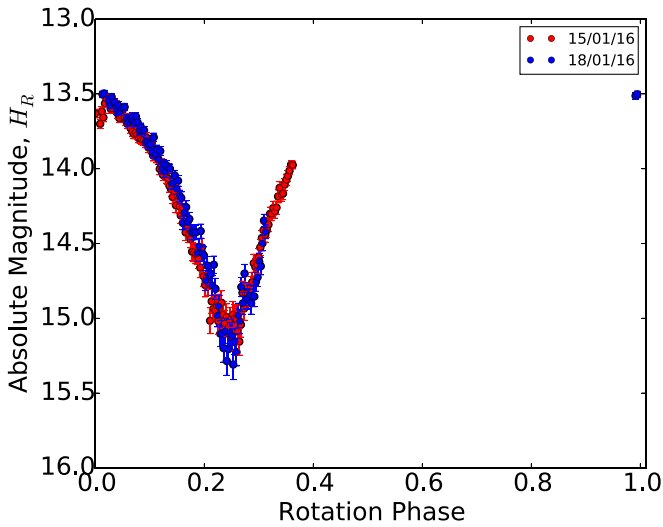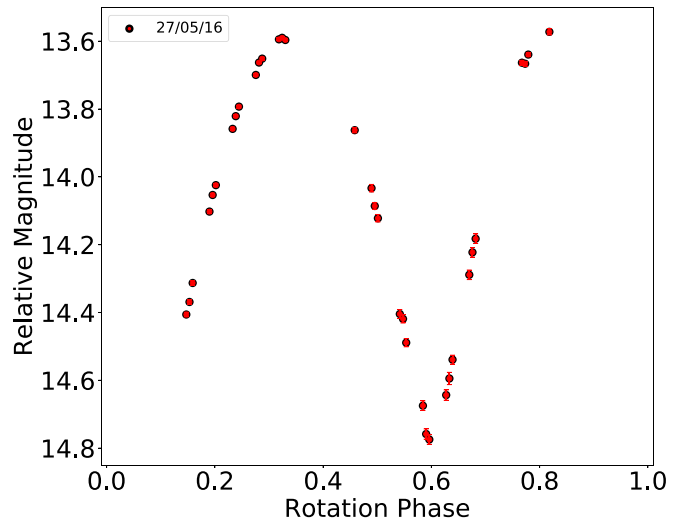
Figure 6. A light curve constructed from photometric data from observations of asteroid 45864 using the University of Hawaii 2.2 m Telescope in 2016 January.
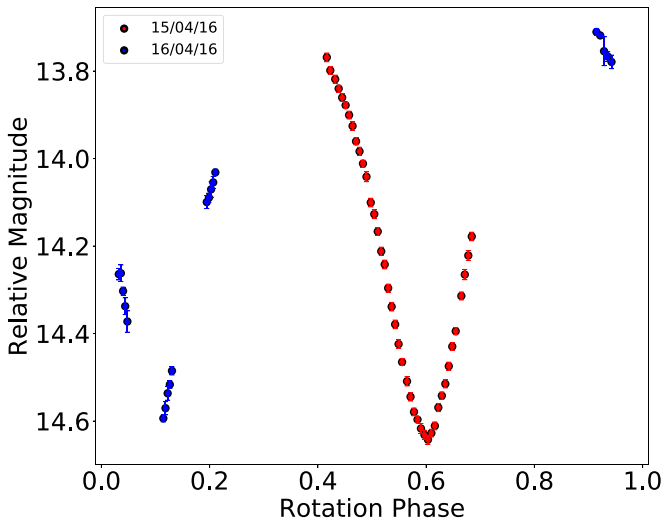

Figure 7. A light curve constructed from photometric data from observations of asteroid 45864 using the Isaac Newton Telescope in 2016 April.
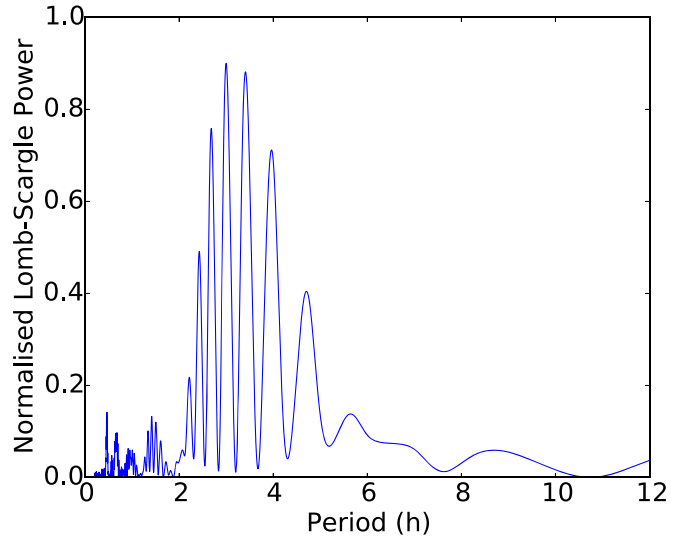

Figure 8. A light curve constructed from photometric data from observations of asteroid 45864 using the University of Hawaii 2.2 m Telescope in 2016 May.

Figure 9. The Lomb–Scargle periodogram generated from the light curve data of 45721.

For an equilibrium figure on the bilobed object sequence rotating with $P_r = 5.135 \pm 0.001$ hr, we find acceptable density solutions across the Ω range from $2600 < \rho < 5200$ kg m^{-3}. These lower ρ values are potentially plausible densities for this asteroid and would imply a less bilobed shape, i.e., $c' \approx c$. Consider the case of the bifurcation ellipsoid with axis ratios 1:0.30:0.27. The amplitude of the light curve for an object of this shape is approximately $A = 1.30$ mag. We also consider the shape on the sequence with the greatest elongation (a/b) with axis ratios 1:0.27:0.24 and a waist axis ratio $c' = 0.23$. Assuming this to have the projected area of a standard ellipsoid, we estimate a light curve amplitude of this object $A_{\mathrm{obs}} = 1.41$ mag, with this value being greater than the actual amplitude that would be produced as we ignore the decrease in projected area of the object caused by its waist. From these estimates, a particularly elongated bilobed shape gives a valid solution for this asteroid.

In summary, we find that it has not been possible to find a simple shape solution for 45864. The large amplitude of the object along with its rotation period would imply that this object cannot exist as a single elongated rubble-pile ellipsoid, and a best fit for a bilobed object using the Roche approximation produced an infeasible density. We are instead forced to consider that this simplification may not be sufficient to explain the structure of 45864. For this object, we consider a single triaxial ellipsoid with axis 1:0.35 $\pm$ 0.01:0.29 $\pm$ 0.01, density $1600 < \rho < 5200$ kg m^{-3}, and minimum internal strength in the range 0–130 Pa to be the most valid solution. We hope to obtain further observational data for this object.

6.3. 45721 (2000 GZ42)

The high-amplitude nature of this object was also observed by *WISE*, and 45721 was identified as a potential target for observational follow-up as a potential close binary asteroid by both Sonnett et al. (2015) and Lacerda et al. (2015). The resulting Lomb–Scargle periodogram is given in Figure 9.

The periodogram shows a best-fit rotation period of $P_r = 6.00 \pm 0.06$ hr with a measured amplitude of 1.11 $\pm$ 0.07 mag. The phase angle of these observations was relatively
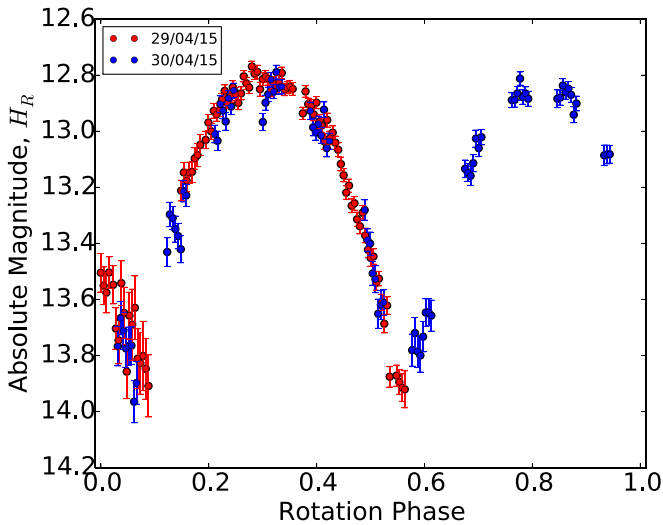
Figure 10. A light curve constructed from photometric data from observations of asteroid 45721 using the Isaac Newton Telescope in 2015 April and phased to the determined rotation period $P_r = 6.00$ hr.

Figure 11. The Lomb–Scargle periodogram generated from the light curve data of 18018.

small ($4°$), and as such any correction to the amplitude is identical within uncertainties. The light curve phased with the best-fit period is given in Figure 10.

The PTF identified this object as having a rotation period of 6.00 ± 0.06 hr (Waszczak et al. 2015), in excellent agreement within the σ of the value that we obtained.

Assuming this object to be a Jacobi ellipsoid, we find that for this spin period and amplitude an object with axis ratios $1{:}0.36 \pm 0.02{:}0.29 \pm 0.02$ and density $\rho = 1600 \pm 100\,\mathrm{kg\,m^{-3}}$ would be required. This is a plausible density for a rubble-pile asteroid, although this shape is close to the critical shape $b/a = 0.43$ at which mass loss would be expected. Assuming an angle of friction $\phi_F = 15°$, we find a range of possible densities explaining this shape and spin rate 1100–$4300\,\mathrm{kg\,m^{-3}}$. For this density range, we then find that cohesive strengths of 0–$120\,\mathrm{Pa}$ provide the best solutions for cohesive strength across this range.

From the Roche model for this object we find a density range $\rho = 2800 \pm 300\,\mathrm{kg\,m^{-3}}$, a plausible range of values for low-porosity chondritic asteroids. However, there is no clear evidence to suggest that a bilobed solution of this kind is any more likely than a single elongated shape solution.

Solving for density along the bilobed equilibrium sequence with rotation rate $P_r = 6.00 \pm 0.06$ hr, we obtain solutions $1900 < \rho < 3800\,\mathrm{kg\,m^{-3}}$. Where c' approaches zero, the density required would be too high to be plausible, exceeding that of solid chondritic chondrite ($3300\,\mathrm{kg\,m^{-3}}$) and potentially requiring a low-porosity metallic composition. However, for larger c' values, the densities are more in line with the known density of asteroids. While a bilobed shape may be a plausible explanation for this object and we have to consider it as such, its amplitude $A_{\mathrm{obs}} = 1.1$ mag may also be more easily explained by a simpler shape, and we have no specific evidence to suggest that this object is likely to be bilobed in nature.

In summary for this object, we find that the observed light curve can be explained by a Jacobi ellipsoid with axis ratios $1{:}0.35 \pm 0.02{:}0.29 \pm 0.02$ and density $\rho = 1600 \pm 100\,\mathrm{kg\,m^{-3}}$. Acceptable explanations with plausible density values may also be obtained for a Roche binary configuration or for a bilobed object. Further observations of this object in the future will be needed to draw any firmer conclusions.
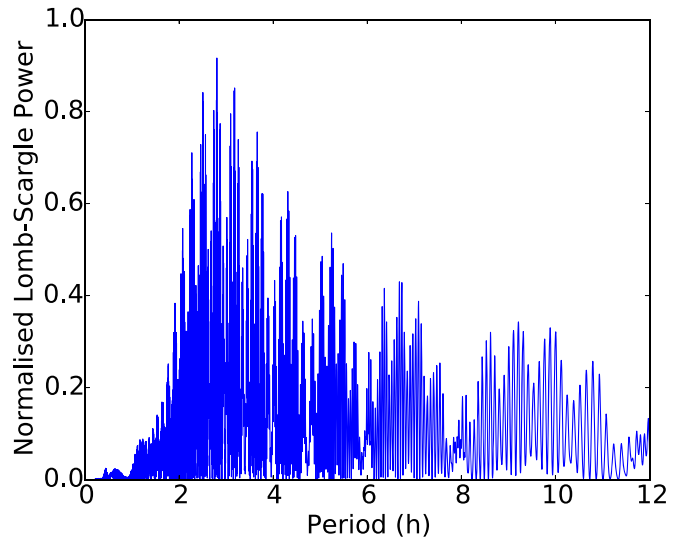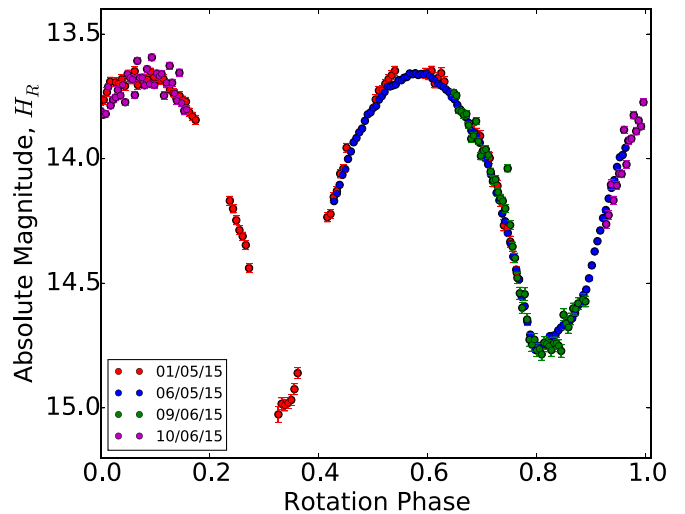

Figure 12. A light curve constructed from photometric data from observations of asteroid 18018 using the Isaac Newton Telescope, University of Hawaii 2.2 m Telescope, and the William Herschel Telescope in 2015 May and phased to the determined rotation period $P_r = 5.608$ hr.

6.4. 18018 (1999 JR125)

The periodogram obtained from our data is presented in Figure 11.

Figure 11 shows a best-fit rotation period of $P_r = 5.608 \pm 0.002$ hr. Light curves folded to this period from the data are given in Figure 12.

The light curve for this object shows an apparent amplitude of $A_{\mathrm{obs}} = 1.33 \pm 0.03$ mag, which when corrected for phase angle is $A = 1.00 \pm 0.03$ mag. Since our observations, the PTF (Waszczak et al. 2015) has reported a rotational period of 5.6077 ± 0.0015 hr for this object, a value in agreement to within uncertainties with our own. From the PTF measurements, an amplitude of 0.77 mag was obtained, a smaller change than that seen in our observations. If indeed this is a reliable value for the amplitude of the light curve, we can infer that the spin-pole axis of this object is not aligned with the orbital plane; however, more data would be needed to get a clearer idea of the object's obliquity.

For an object with this rotation rate and amplitude to be explained by a Jacobi ellipsoid, we find that the ellipsoid must have axis ratios $1:0.40 \pm 0.01:0.32 \pm 0.01$ and a density of $1700 \pm 50 \, \mathrm{kg \, m^{-3}}$. This density is a plausible value; however, the shape of the object would imply that if this body were strengthless that mass loss should occur. For this object to exist as a single Jacobi ellipsoid, some cohesive strength must exist in the object. As for asteroid 45864, we look at the equilibrium figures for ellipsoids with cohesive strength from Holsapple ([2001](#)). Using this shape solution and our measured spin period, we set a limit on the angle of friction encompassing the values for the majority of asteroids $\phi_F < 15°$. Using these values, we find a density range for these equilibrium figures $1200 < \rho < 4800 \, \mathrm{kg \, m^{-3}}$. Using our Drucker–Prager numerical model across this range, we find cohesive strength values in the range 0–160 Pa.

The Roche model of Lacerda & Jewitt ([2007](#)) gave a lower limit density for this system of $\rho = 3300 \pm 100 \, \mathrm{kg \, m^{-3}}$. This density is only believable in the case of a solid chondritic object, not in the case of a rubble-pile asteroid. Solid objects like this would not deform due to mutual gravity and hence would not take the form of a Roche tidally deformed bilobed object. As stated in Section [1.2](#) a binary formed of solid objects without any Roche deformation would be likely to consist of more spherical components and would be unlikely to be able to produce a light curve amplitude as high as the one observed from this object.

Calculating the density of equilibrium figures in the bilobed sequence rotating with this object's rotation period, we find a range of solutions $2200 < \rho < 4400 \, \mathrm{kg \, m^{-3}}$ along the sequence. The lower density values are plausible for this asteroid, suggesting that a bilobed shape may explain the brightness variation of this object as long as c' does not approach zero. These shapes are also capable of producing light curves matching the observed amplitude of 18018. Thus, we consider a bilobed shape to be a possible explanation for the light curve of this object.

In summary, we find possible solutions for both a triaxial ellipsoid with minimum cohesive strength 0–160 Pa, axis ratio $1:0.40 \pm 0.01:0.32 \pm 0.01$, and density $1200 < \rho < 4800 \, \mathrm{kg \, m^{-3}}$ and for a bilobed object, where c' does not approach zero. There is no evidence to suggest either solution to be more likely than the other, and thus we consider the simpler case of the Jacobi ellipsoid to be the more viable fit until more data can be obtained.

6.5. 18280 (4245 T-3)

The periodogram for this data is shown in Figure [13](#).

The best-fit period for 18280 was found to be $P_{\mathrm{LS}} = 1.904 \pm 0.004 \, \mathrm{hr}$ corresponding to a rotation period of $P_r = 3.808 \pm 0.008 \, \mathrm{hr}$ with an observed amplitude of 1.15 ± 0.05 mag. The corrected amplitude for this object was 0.87 ± 0.05 mag, below our cutoff for high-amplitude objects. The phased light curve folded to this rotation period is shown in Figure [14](#)

No other light curve data exist for this object at the time this work was written. Although this object has neither an amplitude above our cutoff nor a rotation period shorter than the spin barrier, its above and below average values, respectively, give us some reason to determine its required strength, if any.
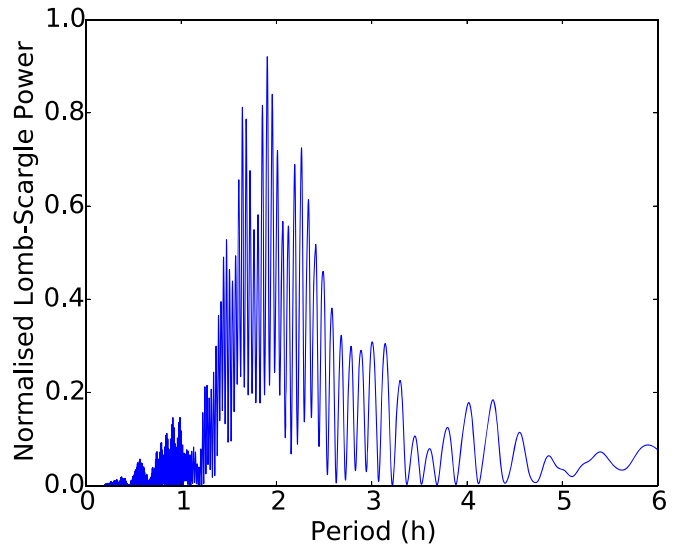

Figure 13. The Lomb–Scargle periodogram generated from the light curve data of 18280.
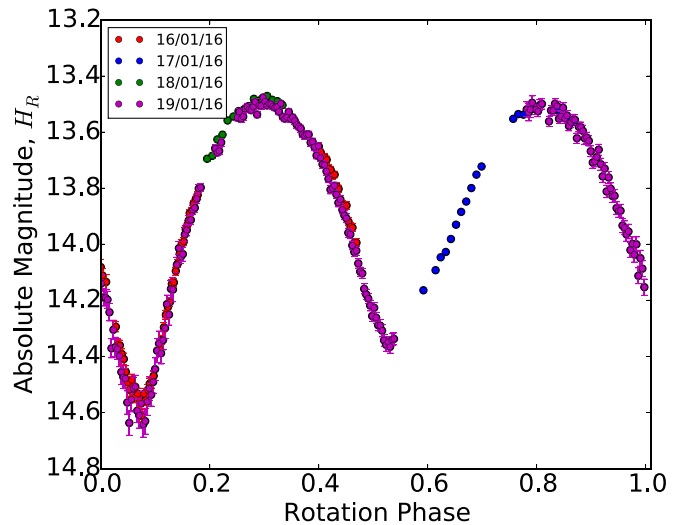

Figure 14. A light curve constructed from photometric data from observations of asteroid 18280 using the Isaac Newton Telescope and the UH2.2 m in 2016 January and phased to the determined rotation period $P_r = 3.808$ hr.

Assuming this object to be a Jacobi ellipsoid, we find a best solution for an object with an axis ratio of $1:0.45 \pm 0.02:0.35 \pm 0.01$ and a density of $\rho = 3500 \pm 100 \, \mathrm{kg \, m^{-3}}$. This shape is slightly less elongated than the limit at which a strengthless body would be expected to undergo mass loss and so this may still be a possible shape for the object. Assuming an angle of friction $\phi_F = 15°$, we find solutions in the density range of $2300 < \rho < 7900 \, \mathrm{kg \, m^{-3}}$ with the upper limit imposed corresponding to the grain density of solid iron, $\rho = 7900 \, \mathrm{kg \, m^{-3}}$. In this range, we find required density-dependent cohesive strengths in the range 0–400 Pa, with strengthless solutions for densities in the range $2500 < \rho < 5000 \, \mathrm{kg \, m^{-3}}$.

Therefore, we conclude that this object is best explained by a single triaxial ellipsoid with density in the range $2600 < \rho < 7900 \, \mathrm{kg \, m^{-3}}$, potentially with some internal cohesive strength if it has a particularly high density, $\rho > 5000 \, \mathrm{kg \, m^{-3}}$.
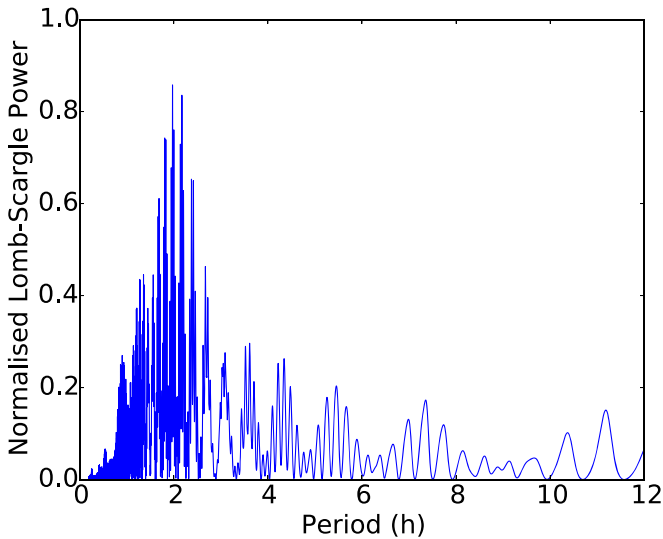
Figure 15. The Lomb–Scargle periodogram generated from the light curve data of 206167.
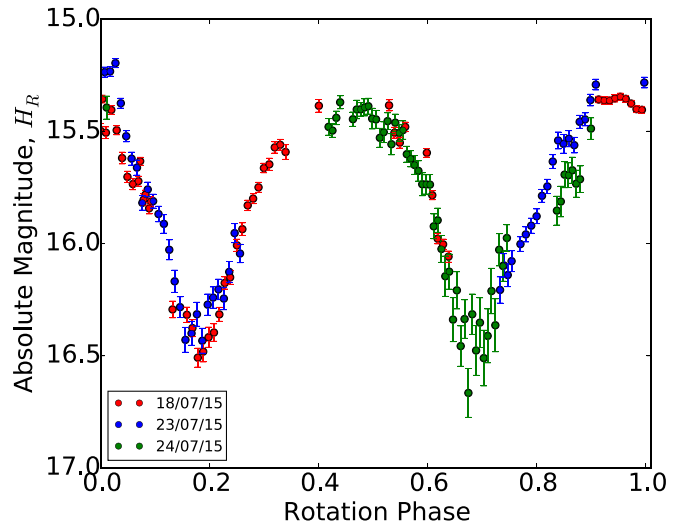

Figure 16. A light curve constructed from photometric data from observations of asteroid 206167 using the NTT and UH2.2 m in 2015 July phased to the determined rotation period $P_r = 3.946$ hr.

6.6. 206167 (2002 TS242)

The Lomb–Scargle periodogram measured for this asteroid is shown in Figure 15.

Figure 15 shows a best-fit rotation period of $P_r = 3.946 \pm 0.006$ hr. The light curve of 206167 folded to this rotation period is shown in Figure 16. Considering the central maximum in Figure 13 to be more reliable than the more scattered maximum, we estimate an amplitude of 1.05 ± 0.15 mag, with this value reducing to 0.86 ± 0.12 mag when phase-angle effects are taken into consideration.

If we assume the object to be a Jacobi ellipsoid, then from Chandrasekhar (1969) we find this is best fit by an object with axis ratio $1:0.45 \pm 0.05:0.36 \pm 0.03$. The density of this object was calculated as $\rho = 3200 \pm 200$ kg m^{-3}. This shape is slightly below the limit at which mass loss would be expected for a strengthless body, and so this may still be a possible shape for the object assuming zero cohesive strength. The density obtained, however, would imply that this object would have to be a monolith of solid chondrite and would hence not take the form of a Jacobi ellipsoid. We therefore consider it highly unlikely that this object is a strengthless Jacobi ellipsoid. Instead, we assume an angle of friction $\phi_F = 15°$ and find a range of possible densities explaining this shape and spin rate 2100–7900 kg m^{-3}. For this density range, we then find that cohesive strengths of 0–350 Pa provide the best solutions for cohesive strength, with strengthless solutions found in the range $2300 < \rho < 3300$ kg m^{-3}.

In conclusion, this asteroid's light curve was best explained by a triaxial ellipsoid with density in the lower end of the range $2600 < \rho < 7900$ kg m^{-3} with axis ratio $1:0.45 \pm 0.05:0.35 \pm 0.03$ and density-dependent required cohesive strength 0–350 Pa.

6.7. 15613 (2000 GH136)

This object was observed for only one night late in the project on 19/04/16 using the INT, during which forty-seven 60 s exposures were taken. The Lomb–Scargle periodogram for the data taken is given as Figure 17.

The best-fit rotation period from Figure 17 was $P_r = 3.3 \pm 0.4$ hr. If this period determination is accurate, then the
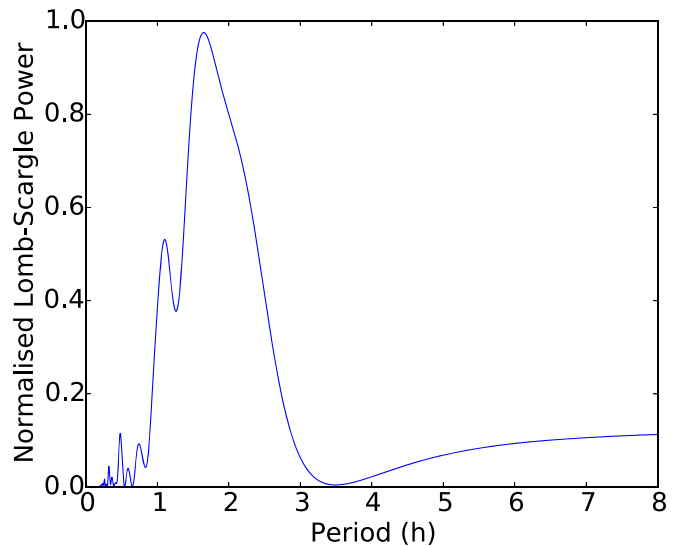
Figure 17. The Lomb–Scargle periodogram generated from the light curve data of 15613.

data we have obtained for this object does not represent a full light curve and further observations will be needed to confirm an accurate period value. The partial light curve obtained folded to the best-fit period is given in Figure 18.

Even in this partial light curve an apparent amplitude of $A = 1.02 \pm 0.02$ mag is seen, although we would require a full light curve containing the second light curve minimum before deeming this the real amplitude. This lower amplitude limit becomes 0.78 ± 0.02 mag when the phase–amplitude relationship is accounted for. The PTF (Waszczak et al. 2015) identified this object as having a rotation period of 3.4184 ± 0.0004 hr, in agreement with the value we obtain from the Lomb–Scargle periodogram. As in the case of 18280, although this object does not meet our cutoff for high-amplitude objects, we calculate its required cohesive strength due to its relatively short rotation period.

In summary, we find that the best solution for a Jacobi ellipsoid producing this light curve is given by the axis ratio $1:0.49 \pm 0.01:0.38 \pm 0.01$ with a density $\rho = 4600 \pm 1100$ kg m^{-3}. Assuming an angle of friction $\phi_F = 15°$, we
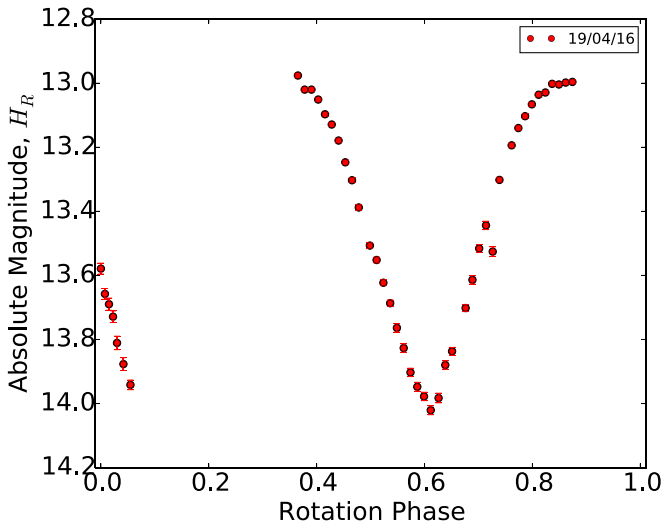
Figure 18. A partial light curve constructed from photometric data from observations of asteroid 15613 using the Isaac Newton Telescope in 2016 April phased to the determined rotation period $P_r = 3.3$ hr.

Figure 19. The Lomb–Scargle periodogram generated from the light curve data of 49257.

find solutions in the density range of $3200 < \rho < 7900 \,\mathrm{kg}\,\mathrm{m}^{-3}$ with the upper limit imposed corresponding to the grain density of solid iron. In this range, we find that the body can be strengthless if its density is $\rho > 3700 \,\mathrm{kg}\,\mathrm{m}^{-3}$; for densities lower than this, strength of up to 250 Pa may be required. It is worth noting that this analysis is based on a partial light curve, and for a more reliable conclusion, further observations of this object would be required.

6.8. 49257 (1998 TJ31)

The Lomb–Scargle periodogram for this object is given in Figure 19.

Figure 19 shows a best-fit rotation period of $P_r = 3.3896 \pm 0.0002$ hr. The light curves for this object phased to this period are given in Figures 20 and 21.

The PTF (Waszczak et al. 2015) reported a rotation period for this object of 3.1661 ± 0.0005 hr, which differs from our obtained value by 7%. This period is listed by the LCDB as having a quality code of 2, defined as a "result based on less than full coverage. Period may be wrong by 30% or ambiguous" (Warner et al. 2009). For comparison, we include a phased light curve of our 2015 July photometric data folded to the rotation period found by PTF in Figure 22. The phase-corrected amplitude of this object was 0.58 ± 0.05 mag, below the cutoff criteria for magnitude above which we consider an asteroid to be truly high amplitude. Despite this, we serendipitously obtained further observations of this object at different orbital geometries, which allowed us to obtain shape and spin data using light curve inversion modeling and found a best-fit model showing that this object is expected to have a higher maximum amplitude than our cutoff. The details of this process will be covered in Section 7.

From our data, we see that the period determined by the PTF does not appear to fit our data, and thus we reject it in favor of our own value, $P_{\rm rot} = 3.3896 \pm 0.0002$ hr.

6.9. Remaining Objects Observed

In addition to the objects considered in the previous section, we observed a further 14 targets throughout the course of the
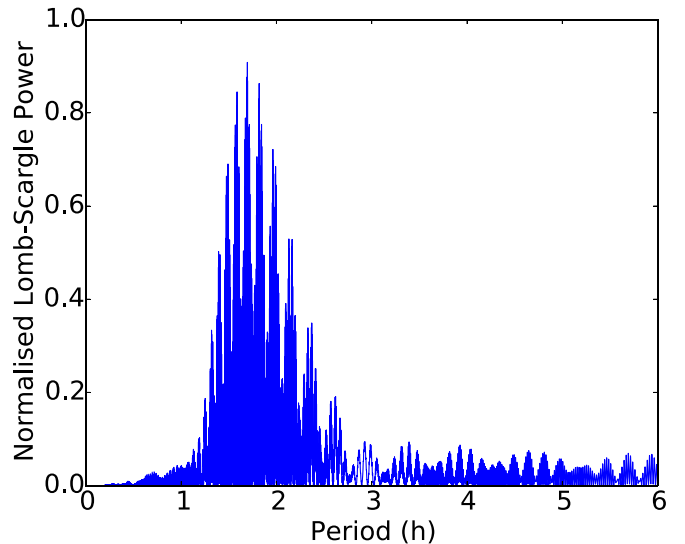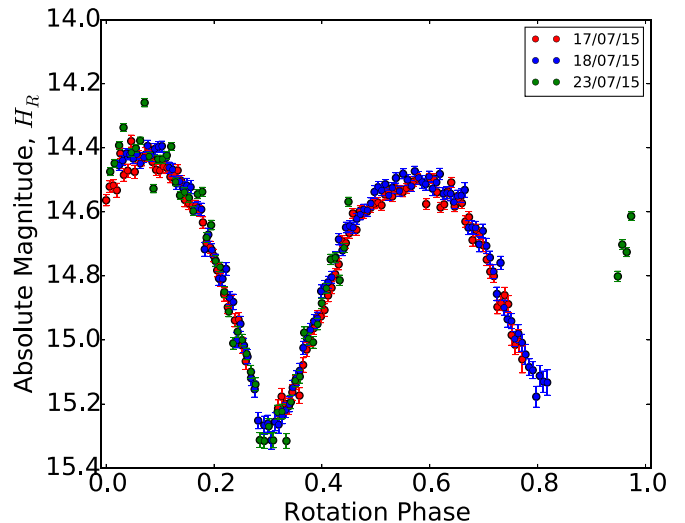

Figure 20. A light curve constructed from photometric data from observations of asteroid 49257 using the NTT and UH2.2 m in 2015 July phase folded to the determined rotation period $P_r = 3.3896$ hr.

project. The orbital parameters as well as the determined periods and amplitudes are given in Table 4. Of these objects, only two can truly be considered to have been false positives in our target list as their rotation period determined either by us or by PTF is too long to have ever produced a change of 0.3 mag in 15 minutes. For the remainder of our targets, it is impossible to state definitively whether these targets are truly high amplitude or not, as we do not know anything about their spin-pole orientation. In these cases, their rotational periods are sufficiently short to have produced a large variation in magnitude if these objects have a higher amplitude than measured from our observations. This could be as a result of PS1 observing the target equator-on or at least closer to this angle than for our own observations.

Although we may find an object to have an apparent amplitude of less than 1 mag, the object may still be high amplitude and the observed amplitude may be due to orbital geometry. As such, we are unable to definitively rule out objects as high amplitude without further data. In the case of all
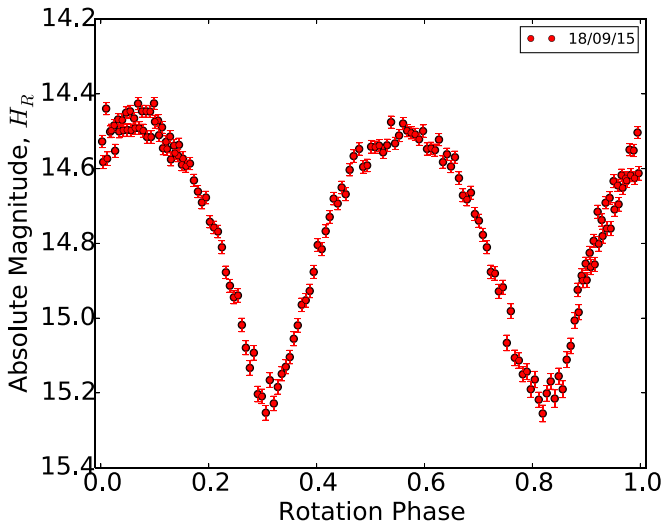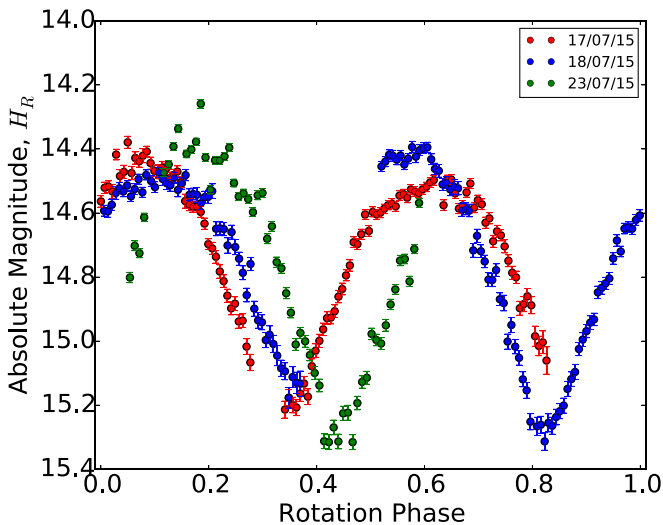
Figure 21. A light curve constructed from photometric data from observations of asteroid 49257 using the UH2.2 m in 2015 September.

Figure 22. A light curve constructed from photometric data from observations of asteroid 49257 using the NTT and UH2.2 m in 2015 July phase folded to the rotation period determined by the Palomar Transient Factory, $P_{PTF} = 3.1661$ hr.

Table 4
Overview of Other Objects Observed during this Project

Object	Period (hr)	Amplitude (mag)
23314	6.2104 ± 0.0004	0.87
81847	4.930 ± 0.002	0.86
140666	3.5 ± 0.1	0.7
55125	5 ± 0.2	0.7
5929	3.76 ± 0.01	0.6
3764	>4	>0.5
12582	∼4	0.4
172388	∼8–10	0.3
56656	2.7	0.25
114372	3.5	0.2
112815	…	…
173046	…	…
15354	…	…
85298	…	…

targets observed, we require a second set of observations at different orbital geometries ideally 90° along their orbit from previously observed in order to show that they are not high-amplitude asteroids. Using the shape distribution for small main belt asteroids from McNeill et al. (2016), we estimate that as many as 0.6% of objects in this size range may produce light curve amplitudes $A \geqslant 1.0$ mag.

6.10. Limitations

Our selection criteria and observational strategy are not without their limitations. As stated earlier, from the sparse data alone, it is impossible to determine in advance whether an object showing large rates of change in magnitude is an object with a fast rotation rate or a high-amplitude light curve. Knowing this would allow us to much more easily optimize our observing strategy for each object and make more efficient use of our time. However, with the data available, this is an unsolvable problem so we have simply had to adapt "on the fly" during our observing runs.

It is also not immediately clear when we observe an object that we can definitively rule out that it is a high-amplitude object. For some of our remaining objects, we obtained light curve amplitudes $A < 0.8$ mag, but without further data there is no way to tell whether these objects actually have a lower amplitude than we are interested in, or if the observing geometry is simply such that we are not seeing the full extent of the amplitude in our light curve due to the spin-pole axis of the asteroid. Following up on these objects would be time consuming and potentially inefficient. We also looked at the difference in true anomaly between the objects when they were observed by us at the telescopes and when they were observed by Pan-STARRS. If there is a change approaching 90° or 270°, then this may suggest that the difference in observed amplitude is due to orbital geometry but there is still no way to conclusively state this without further data. During the project to date, we did not perform any follow-up observations for objects with observed $A < 0.8$ mag, but this may present a useful avenue for further work as similar to the case of 5929 we would expect that some of these seemingly less interesting objects are in fact high amplitude after all. It is worth noting that any objects for which we determined a period $P > 10$ hr is unlikely to really be a high-amplitude object if we see only a low-amplitude light curve. This is because for an object with a period greater than this to produce the sort of magnitude variations we look for as our selection criteria, an unphysical amplitude would be required. It is not known whether these large changes are simply the effect of contamination or are a real effect due to some outside factor, but for our purposes we consider these objects to be false positives.

An interesting finding also is that there appeared to be no clear correlation between the maximum $\dot{m}$ found from the Pan-STARRS data and the extent of the light curve amplitude observed, at least at higher values. Initially we used this value to determine the order we would proceed through our target list, but after two observing runs and no clear correlation, we altered our strategy to instead try and observe as many of our targets as possible rather than simply focusing on a single target that showed a large value of $|\dot{m}|$ in the survey data. Instead, it appears as though the likelihood of an object being high amplitude is independent of the maximum rate of change in magnitude observed, where $\dot{m}_{max} > 0.6$ mag per 15 minutes. This is likely
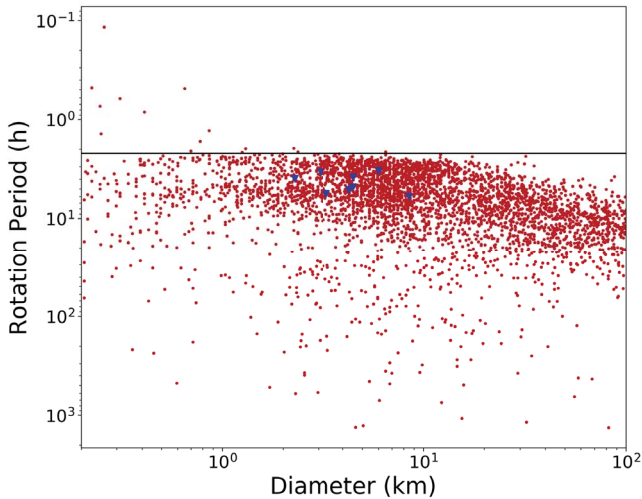
Figure 23. The rotation period and diameter of the eight primary objects (blue points) analyzed in Section 5 shown on the same axes as the corresponding data from the Light Curve Database for all objects $0.2 < D < 100$ km.

Figure 24. The amplitude and rotation period of the eight primary objects (blue points) analyzed in Section 5 compared to known data from the Light Curve Database for objects $0.2 < D < 100$ km. Note that the amplitudes from the LCDB are not corrected for phase angle. The green and magenta lines show the critical spin period for objects with bulk densities $\rho = 2000$ kg m^{-3} and $\rho = 3000$ kg m^{-3}, respectively.

due to the difference in orbital geometry between the PS1 detections of the object and our follow-up observations.

6.11. Summary of Observations

In this project, we have carried out observations of 22 asteroids from our target selection list. In this section, we have detailed the observations and analysis of eight objects considered to be closest to our definition of "extreme asteroids." Figure 23 shows these objects plotted on the same period–diameter axes as the information from the LCDB shown in Figure 1. Clearly, none of our objects have periods shorter than the spin barrier and hence none can be considered large superfast rotators.

Figure 24 shows the amplitudes and rotation periods of these eight objects along with the same information for objects in the LCDB. Also shown are the critical spin periods for objects with $\rho = 2000$ kg m^{-3} and $\rho = 3000$ kg m^{-3}. Here we see that the eight objects studied here do not exceed the given critical spin rates given their density. We find that depending on their density that these objects may still require some cohesive strength, but these values are similar to or lower than known values for asteroid cohesive strengths.

From the data available to us from the Pan-STARRS 1 Survey, we have not identified any objects with superfast rotation or high amplitude requiring unusually high cohesive strength.

7. Shape Modeling

7.1. Light Curve Inversion

Only a small proportion of asteroids have known shapes as obtained by radar observations or resolved from images. These methods are also preferentially biased toward large and/or nearby objects. For most objects, the best method of obtaining shape and spin-pole information is through the use of light curve inversion. This method allows for an approximate shape to be determined as radar imaging of main belt asteroids has revealed objects with large-scale concave features which cannot be reproduced by light curve inversion (Hudson & Ostro 1999; Hudson et al. 2000). In addition to this, it is
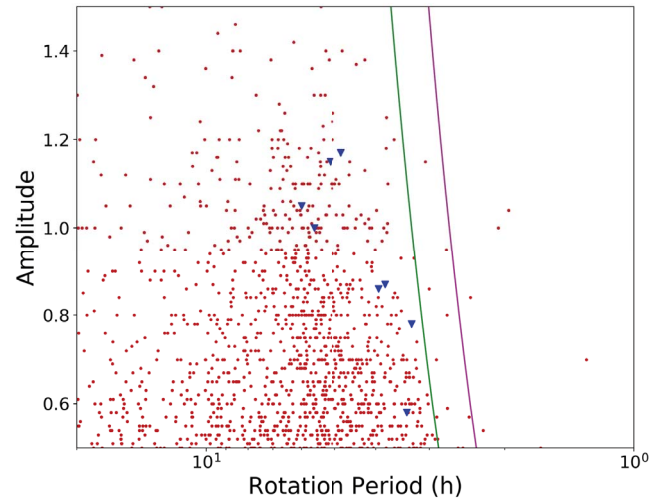
difficult to determine a unique spin-pole solution, as two solutions will generally be found with approximately the same latitude and longitude values separated by 180°. A typical approach to light curve inversion is to place shape constraints on the modeled objects, for instance allowing only minor deviations from a triaxial ellipsoid. To obtain shape and spin models for those asteroids with sufficient observations, we utilize the light curve inversion method devised by Kaasalainen & Torppa (2001) using the software package developed by Durech et al. (2010),

$$dL = S(\mu, \mu_0)\bar{\omega}ds. \qquad (25)$$

The total brightness of an asteroid, L, can be expressed as a function of the shape, surface scattering, and rotation state of the object. The change in the total brightness of the asteroid over time is dependent on the evolution of each of these parameter sets with time. By summing the model values of dL from each surface facet of the modeled object, the value of the brightness for a series of variable parameters, L_{mod} can be determined. We compared this model value with the observed light curve and minimize the chi-squared for a variety of shape and scattering configurations as $\chi^2 = ||L_{\mathrm{obs}} - L_{\mathrm{mod}}||^2$.

During this investigation, we obtained enough observations at different orbital longitudes to allow shape modeling for three of our targets: 45864, 206167, and 49257. In this section, the preliminary shape results for each of these objects are discussed.

7.2. 45864 (2000 UO97)

Using light curve inversion, the best-fit shape generated for 45864 is presented in Figure 25. The model object has approximate axis ratios 1:0.31:0.31, and its best-fit spin-pole longitude and latitude are given by $\beta = 218° \pm 5°$, $\theta = -82° \pm 5°$. This shape is less elongated in terms of axis ratio than the object determined in Section 6.2 as this inversion method does not assume a triaxial ellipsoid and additionally accounts for illumination effects such as limb darkening. This less elongated shape would allow the object to resist rotational

Figure 25. The output shape model of 45864 at two points about its rotation separated by 90°. The object is aligned at its obtained spin-pole latitude $\beta = -82°$.
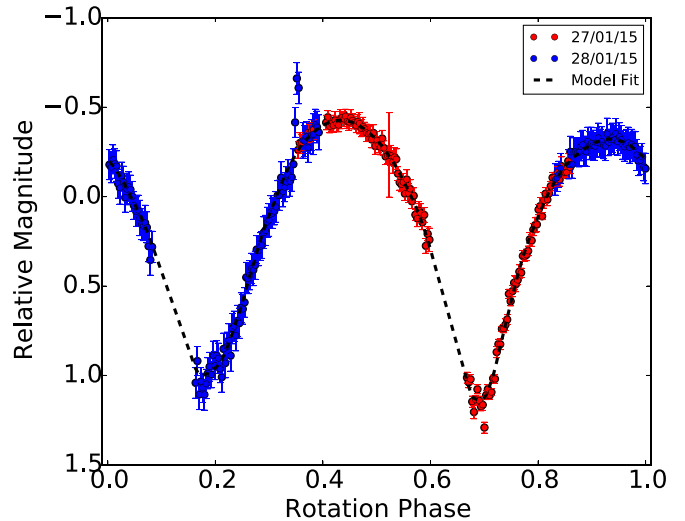

Figure 26. The same light curve as shown in Figure 5. The black line represents the estimated photometric light curve of the output shape model seen in Figure 25.

fission at lower strength values than those obtained for the previous shape. The density range for the object would presumably also change but without a more advanced model, it is not possible to calculate these values, as the work in Section 6.2 assumed a simple triaxial ellipsoid.

The best-fit light curve produced by this model is plotted along with the observed light curves from the 2015 January observations in Figure 26.

Ďurech et al. (2016) used sparse photometry from archival data from the Lowell Observatory to construct shape and spin models for 328 new asteroids in addition to the ∼350 that were previously available on the Database of Asteroid Models from Inversion Techniques (DAMIT; Durech et al. 2010). This added sample included best-fit models of 45864, which are shown in Figures 27(a) and (b). The object was determined to have spin parameters $\lambda = 179°$, $\beta = -84°$ for (a) and $\lambda = 44°$, $\beta = -66°$ for (b). Neither of these shape models would generate the light curves obtained from our observations, and given the dense nature of our photometry, we favor our own fit. The spin-pole latitude obtained from our model, $\beta = -82° \pm 5°$, is in excellent agreement with the first Ďurech fit. Further data will allow us to constrain the shape and spin state information of this object even further, and we hope to obtain observations at at least one more apparition in the future.

7.3. 206167 (2002 TS242)

Asteroid 206167 was observed by our program to have rotation period $P_r = 3.946 \pm 0.006$ and a maximum observed amplitude $A_{\mathrm{obs}} = 1.07 \pm 0.05$. Additional observations of this object in 2016 July gave sufficient observations at different orbital geometries to allow a shape model to be determined. The shape model obtained for this asteroid is shown in Figure 28 with best-fit spin-pole axes $\lambda = 57° \pm 5°$, $\beta = -67° \pm 5°$.

The light curve produced by the shape model is plotted along with the 2015 July NTT observations in Figure 29. At the time of writing, there are no shape or spin-pole models for this object for comparison.

7.4. 49257 (1998 TJ31)

Asteroid 49257 was observed to have a light curve amplitude below the selection criterion decided for high-amplitude objects. Despite this, we serendipitously obtained further observations of this object at different orbital geometries, which allowed us to obtain shape and spin data. The best-fit shape result for this object is given in Figure 30, with best-fit spin-pole longitude and latitude $\beta = 112° \pm 5°$, $\theta = 6° \pm 5°$. The relative light curve that
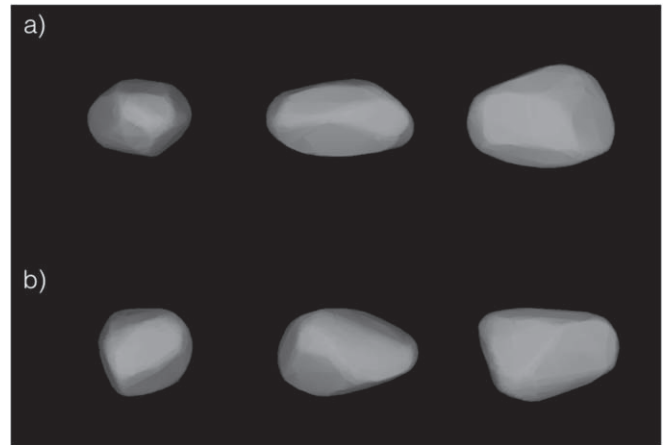
Figure 27. The best-fit shape solutions for 45864 as listed in DAMIT (Ďurech et al. 2016). (a) A best-fit shape with spin-pole longitude and latitude $\lambda = 179°$, $\beta = -84°$. (b) A best-fit shape with spin-pole longitude and latitude $\lambda = 44°$, $\beta = -66°$.
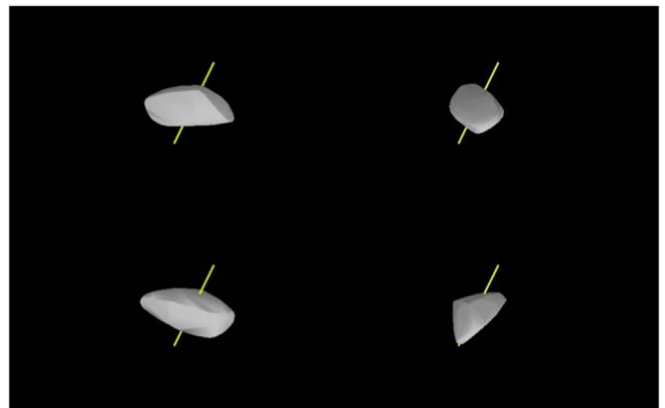

Figure 28. The output shape model of 206167 at four points about its rotation separated by 90°. The object is aligned at its obtained spin-pole latitude $\beta = -67° \pm 5°$.
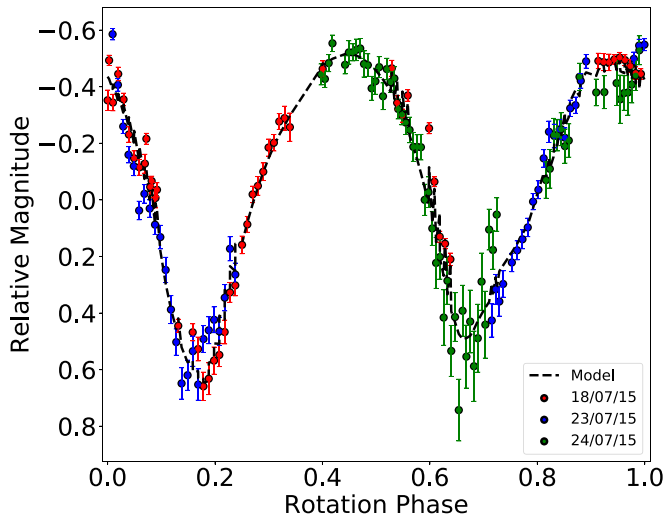
Figure 29. A light curve constructed from photometric data from observations of asteroid 206167 using the NTT in 2015 July. The black dotted line is the light curve obtained from the shape model given in Figure 28.

Figure 30. The output shape model of 49257 at four points about its rotation separated by 90°. The object is aligned at its obtained spin-pole latitude $\beta = 6°$.

Figure 31. A light curve constructed from photometric data from observations of asteroid 49257 using the UH2.2m in 2015 September. The black dotted line is the light curve obtained from the shape model given in Figure 30.

would be obtained from this shape is plotted alongside the measured light curve from this object in Figure 31.

The light curve produced by this model object is plotted along with the observed light curve from observations in 2015 July in Figure 26.

We see that the model shape fits the observed light curve fairly well in this case. It is also interesting to note that if this shape is accurate, then if we observe the object "edge-on," we would expect to see a greater light curve amplitude. We hope to obtain further data for this object. At the time of writing, there was no pre-existing shape or spin-pole information for asteroid 49257 to use for comparison. The spin-pole solution for this object suggests a high obliquity; Lacerda (2011) demonstrated that the light curve amplitude of a high-obliquity object can vary greatly about its orbital geometry, and this could explain why this object was not determined to be an "extreme asteroid" despite the shape solution suggesting a higher amplitude than measured in our project.

8. Conclusions

Using the first 18 months of the Pan-STARRS 1 survey, we identified 33 candidate high-amplitude objects for follow-up observations and carried out observations of 22 asteroids. Four of the observed objects have amplitude $A_{obs} \geqslant 1.0$ mag. Despite the fact that our selection criteria was initially defined for identification of asteroids with fast rotation periods, $P < 2.2$ hr, we found none of these "superfast rotators" in our target list. Of the remaining observed objects for which light curve amplitudes $A_{obs} < 0.9$ mag were obtained, we are only able to definitively rule two out as high-amplitude targets. The rotation periods we determine from the light curves of these asteroids were too long for the large variations seen in the PS1 survey data to be real without assuming an unrealistic amplitude. In future work, we hope to obtain photometric colors and/or spectroscopy for these objects which will allow us to further constrain their density and strengths. Additionally, knowing the taxonomic type of the asteroid will allow us to more accurately account for the phase-angle amplitude effect.

Asteroid 49257 was observed by our project to have an amplitude lower than our cutoff criteria. When we obtained enough further observational data for this objects to generate a
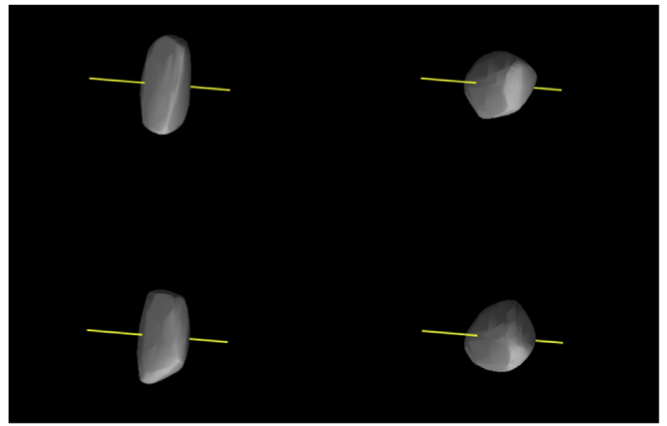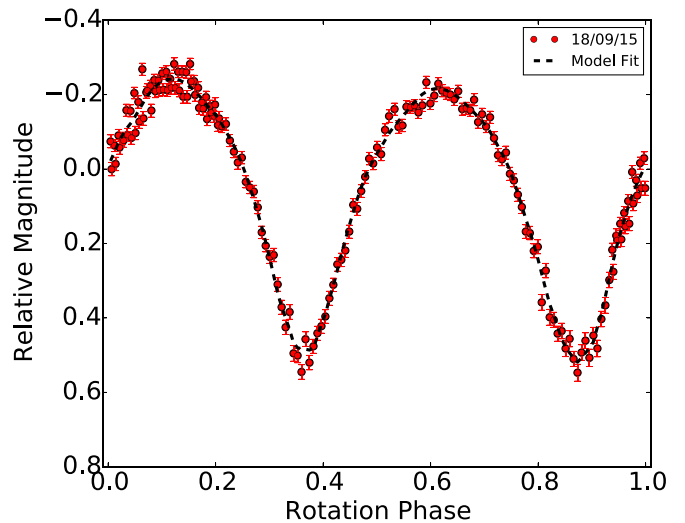
shape model, however, we found that the best-fit shape would be considered a high-amplitude asteroid. At least one further set of observations at different orbital geometries is required to rule any of our targets out as high-amplitude asteroids. Assuming the shape distribution determined in McNeill et al. (2016), we find that as many as 0.6% of main belt asteroids with $1 < D < 10$ km may be high-amplitude objects with $A_{max} \geqslant 1.0$ mag. From this investigation, we find four asteroids out of 22 total observed to have amplitudes $A \geqslant 1.0$ mag. We can use this to estimate an expected lower limit on the abundance of high-amplitude asteroids within survey data. Scaling the proportion of high-amplitude asteroids observed to our master target list, we estimate that from the full PS1 sample of ∼60,000 objects we would expect 0.01% to be high amplitude. This number is not particularly constraining as it only represents an estimate of the lower limit abundance of high-amplitude asteroids.

We determine that the four objects are likely to be single rubble-pile objects with some cohesive strength allowing them to resist mass shedding even at their highly elongated shapes, depending on their density. Three further objects below the cutoff for "high-amplitude asteroids" had a combination of amplitude and period such that they may also require some

density-dependent cohesive strength. None of these objects require any strength significantly greater than the determined values for known asteroids to date. It is also worth noting that increasing the angle of friction used in the calculations will reduce these values further (Sánchez & Scheeres 2016). Thus, although these objects display higher than average amplitude, due to the relatively small internal strengths required to resist rotational fission, none are considered extraordinarily high amplitude.

For asteroids 45864, 206167, and 49257 in our program, we had obtained enough data at different epochs and orbital geometries to allow us to model the shape and spin-pole orientation of these objects. Asteroid 45864 was determined to have retrograde rotation with spin-pole latitude and longitude $\lambda = 218° \pm 10°$, $\beta = -82° \pm 5°$ and 206167 with $\lambda = 57° \pm 5°$, $\beta = -67° \pm 5°$. Asteroid 49257 was determined to have a spin pole at $\lambda = 112° \pm 6°$, $\beta = 6° \pm 5°$. The high obliquity of 49257 could explain how we failed to identify this body as high amplitude from its light curve alone when its shape solution suggests otherwise as the light curve amplitude of high-obliquity objects is highly dependent on orbital geometry.

Facilities: Pan-STARRS 1; Isaac Newton Telescope, La Palma; New Technology Telescope, La Silla, Chile; University of Hawaii 2.2m Telescope.

Software: astropy (Astropy Collaboration et al. 2013).

ORCID iDs

Alan Fitzsimmons https://orcid.org/0000-0003-0250-9911
Robert Jedicke https://orcid.org/0000-0001-7830-028X
Pedro Lacerda https://orcid.org/0000-0002-1708-4656
David E. Trilling https://orcid.org/0000-0003-4580-3790
Ernst DeMooij https://orcid.org/0000-0001-6391-9266
Matthew J. Hooton https://orcid.org/0000-0003-0030-332X

References

Alejano, L., & Bobet, A. 2012, RMRE, 45, 995
Astropy Collaboration, Robitaille, T. P., Tollerud, E. J., et al. 2013, A&A, 558, A33
Benner, L. A. M., Nolan, M. C., Ostro, S. J., et al. 2006, Icar, 182, 474
Bottke, W. F., Jr., Cellino, A., Paolicchi, P., & Binzel, R. P. 2002, in Asteroids III (Tucson, AZ: Univ. Arizona Press), 3
Chambers, K. C., Magnier, E. A., Metcalfe, N., et al. 2016, arXiv:1612.05560
Chandrasekhar, S. 1963, ApJ, 138, 1182
Chandrasekhar, S. 1969, Ellipsoidal figures of equilibrium
Chandrasekhar, S., & Lebovitz, N. R. 1962, ApJ, 136, 1037
Chang, C.-K., Ip, W.-H., Lin, H.-W., et al. 2015, ApJS, 219, 27
Chang, C.-K., Lin, H.-W., Ip, W.-H., et al. 2016, ApJS, 227, 20
Cook, A. F., Hemenway, C . L., & Millman, P. M. 1971, BAAS, 3, 369
Cruikshank, D. P., Dalle Ore, C. M., Roush, T. L., et al. 2001, Icar, 153, 348
Davis, L. E. 1999, in ASP Conf. Ser. 189, Precision CCD Photometry, ed. E. R. Craine, D. L. Crawford, & R. A. Tucker (San Francisco, CA: ASP), 35
Denneau, L., Jedicke, R., Grav, T., et al. 2013, PASP, 125, 357
Descamps, P. 2015, Icar, 245, 64
Descamps, P., Marchis, F., Michalowski, T., et al. 2007, Icar, 189, 362
Dunlap, J. L., & Gehrels, T. 1969, AJ, 74, 796
Durda, D. D., Bottke, W. F., Enke, B. L., et al. 2004, Icar, 170, 243
Ďurech, J., Hanuš, J., Oszkiewicz, D., & Vančo, R. 2016, A&A, 587, A48
Durech, J., Sidorin, V., & Kaasalainen, M. 2010, A&A, 513, A46
Flewelling, H. A., Magnier, E. A., Chambers, K. C., et al. 2016, arXiv:1612.05243
Holsapple, K. A. 2001, Icar, 154, 432
Holsapple, K. A. 2004, Icar, 172, 272
Holsapple, K. A. 2007, Icar, 187, 500
Horne, J. H., & Baliunas, S. L. 1986, ApJ, 302, 757
Howell, S. B. 1989, PASP, 101, 616
Hudson, R. S., & Ostro, S. J. 1999, Icar, 140, 369
Hudson, R. S., Ostro, S. J., Jurgens, R. F., et al. 2000, Icar, 148, 37
Jeans, J. H. 1919, Problems of cosmogony and stellar dynamics
Kaasalainen, M., & Torppa, J. 2001, Icar, 153, 24
Lacerda, P. 2011, AJ, 142, 90
Lacerda, P., Ali-Lagoa, V., Licandro, J., & Peixinho, N. 2015, in European Planetary Science Congress, EPSC2015-691
Lacerda, P., & Jewitt, D. C. 2007, AJ, 133, 1393
Lacerda, P., McNeill, A., & Peixinho, N. 2014, MNRAS, 437, 3824
Leone, G., Paolicchi, P., Farinella, P., & Zappala, V. 1984, A&A, 140, 265
Magnier, E. A., Chambers, K. C., Flewelling, H. A., et al. 2016, arXiv:1612.05240
Magnier, E. A., Schlafly, E., Finkbeiner, D., et al. 2013, ApJS, 205, 20
Mainzer, A., Grav, T., Masiero, J., et al. 2011, ApJ, 741, 90
Mann, R. K., Jewitt, D., & Lacerda, P. 2007, AJ, 134, 1133
Marchis, F., Hestroffer, D., Descamps, P., et al. 2005, Icar, 178, 450
Masiero, J. R., Mainzer, A. K., Grav, T., et al. 2011, ApJ, 741, 68
McNeill, A., Fitzsimmons, A., Jedicke, R., et al. 2016, MNRAS, 459, 2964
Nesvorný, D., Vokrouhlický, D., Bottke, W. F., Noll, K., & Levison, H. F. 2011, AJ, 141, 159
Ostro, S. J., Hudson, R. S., Nolan, M. C., et al. 2000, Sci, 288, 836
Polishook, D., Moskovitz, N., Thirouin, A., et al. 2017, Icar, 297, 126
Polishook, D., Moskovitz, N., Binzel, R. P., et al. 2016, Icar, 267, 243
Pravec, P., Harris, A. W., & Michalowski, T. 2002, in Asteroids III, ed. W. F. Bottke, Jr. et al. (Tucson, AZ: Univ. Arizona Press), 113
Pravec, P., Scheirich, P., Kušnirák, P., et al. 2006, Icar, 181, 63

Pravec, P., Vokrouhlický, D., Polishook, D., et al. 2010, Natur, 466, 1085
Rozitis, B., & Green, S. F. 2014, A&A, 568, A43
Sánchez, P., & Scheeres, D. J. 2016, Icar, 271, 453
Sharma, I., Jenkins, J. T., & Burns, J. A. 2009, Icar, 200, 304
Shepard, M. K., Taylor, P. A., Nolan, M. C., et al. 2015, Icar, 245, 38
Sheppard, S. S., & Jewitt, D. 2004, AJ, 127, 3023
Sonnett, S., Mainzer, A., Grav, T., Masiero, J., & Bauer, J. 2015, ApJ, 799, 191
Taylor, P. A., & Margot, J.-L. 2011, Icar, 212, 661

Tonry, J. L., Stubbs, C. W., Lykke, K. R., et al. 2012, ApJ, 750, 99
Usui, F., Kuroda, D., Müller, T. G., et al. 2011, PASJ, 63, 1117
Warner, B. D., Harris, A. W., & Pravec, P. 2009, Icar, 202, 134
Waszczak, A., Chang, C.-K., Ofek, E. O., et al. 2015, AJ, 150, 75
Weidenschilling, S. J. 1980, Icar, 44, 807
Zappala, V., Cellino, A., Barucci, A. M., Fulchignoni, M., & Lupishko, D. F. 1990, A&A, 231, 548
Zechmeister, M., & Kürster, M. 2009, A&A, 496, 577